The heterogeneous distribution of extracellular adenosine reveals a myeloid-dependent axis, shaping the immunosuppressive microenvironment in pancreatic ductal adenocarcinoma

Vincenzo Graziano[1,2], Andreas Dannhorn[3*], Heather Hulme[3*], Kate Williamson[4*], Hannah Buckley[1], Sheng Y. Lee[1], Brajesh P. Kaistha[1#], Sabita Islam[1,2,5], James E. D. Thaventhiran[4], Frances M. Richards[1°] Richard Goodwin[3], Rebecca Brais[6], Simon J. Dovedi[7], Alwin G. Schuller[8], Jim Eyles[7], Duncan I. Jodrell[1,5]

[1]Cancer Research UK Cambridge Institute, University of Cambridge, Cambridge, UK

[2]Cancer Research UK Cambridge Centre, University of Cambridge, Cambridge, UK

[3]Imaging and Data Analytics, Clinical Pharmacology and Safety Sciences (CPSS), AstraZeneca, Cambridge, UK

[4]Medical Research Council Toxicology Unit, University of Cambridge, Cambridge, CB2 1QW, UK

[5]Department of Oncology, University of Cambridge, Cambridge UK

[6]Department of Pathology, Cambridge University Hospitals NHS Foundation Trust, CB2 0QQ Cambridge, UK.

[7]Oncology R&D, Research and Early Development, AstraZeneca, Cambridge, UK

[8]Oncology R&D, Research and Early Development, AstraZeneca, Waltham, USA

[*] These authors contributed equally to this work

Brajesh P. Kaistha current address: Oncology R&D, Research and Early Development, AstraZeneca Cambridge, UK

° Frances M. Richards current address: Oncology R&D, Translational Medicine, AstraZeneca, Cambridge, UK

Running title

Extracellular adenosine controls the immunosuppressive microenvironment of PDAC

Keywords

Pancreatic cancer, adenosine pathway, immunotherapy, pro-tumorigenic macrophages, tumour microenvironment

Financial support:

All CRUK CI authors received research funding from Cancer Research UK (Nos. C14303/A17197 and C9545/A29580). The Li Ka Shing Centre where this work was performed was generously funded by CK Hutchison Holdings Limited, the University of Cambridge, CRUK, The Atlantic Philanthropies and others. This work was supported by Cancer Research UK (C9685/A27444) to VG. This study was also funded by Cancer Research UK Precision Panc grant C96/A25238. HB is funded by the University of Cambridge Experimental Medicine Training Initiative programme in partnership with AstraZeneca (EMI-AZ) and SYL is funded by the Cambridge Trust (Cambridge International Scholarship). Work by JT and KW is funded by a core grant award from the MRC (MC_UU_00025/12).

Corresponding authors:

Vincenzo Graziano: Cancer Research UK Cambridge Institute, University of Cambridge, Li Ka Shing Centre, Robinson Way, Cambridge, CB2 0RE, United Kingdom. Email: vincenzo.graziano@cruk.cam.ac.uk

Duncan Jodrell: Cancer Research UK Cambridge Institute, University of Cambridge, Li Ka Shing Centre, Robinson Way, Cambridge, CB2 0RE, United Kingdom; Department of Oncology, University of Cambridge, Cambridge, CB2 0XZ, United Kingdom. Email: dij21@cam.ac.uk

Authors' disclosures:

AD, HH, BPK, FMR, RG, SJD, AGS and JE are Astrazeneca employees and own company stocks and shares. HB holds a studentship partially funded by Astrazeneca.

Abstract

The prognosis for patients with pancreatic ductal adenocarcinoma (PDAC) remains extremely poor. It has been suggested that the adenosine pathway contributes to the ability of PDAC to evade the immune system and its resistance to immunotherapies (Immuno-Oncology Therapy, IOT), by generating extracellular adenosine (eAdo).

Using syngeneic genetically engineered mouse allograft models of PDAC with differential immune infiltration and response to IOT, we showed enrichment of the adenosine pathway in tumour-infiltrating immune cells (in particular, myeloid populations). Extracellular adenosine distribution is heterogeneous in tumours, with high concentrations in hypoxic margins that surround necrotic areas, associated with a rich myeloid infiltration. Pro-tumorigenic M2 macrophages express high levels of the Adora2a receptor; particularly in the IOT resistant model. Blocking the *in vivo* formation and function of eAdo (Adoi), using a combination of anti-CD73 antibody and an Adora2a inhibitor slowed tumour growth and reduced metastatic burden. In addition, blocking the adenosine pathway improved the efficacy of combinations of cytotoxic agents or immunotherapy. Finally, Adoi remodelled the tumour microenvironment (TME), as evidenced by reduced infiltration of M2 macrophages and Tregs. RNAseq analysis showed that genes related to immune modulation, hypoxia and tumour stroma were downregulated following Adoi and a specific adenosine signature derived from this is associated with a poorer prognosis in PDAC patients.

The formation of eAdo appears to promote the development of the immunosuppressive TME in PDAC, contributing to its resistance to conventional and novel therapies. Therefore, inhibition of the adenosine pathway may represent a strategy to modulate the stroma and improve therapy response in patients with PDAC.

Introduction

Survival for patients with pancreatic ductal adenocarcinoma (PDAC) has not changed significantly in the last 50 years and remains poor (https://www.cancerresearchuk.org/health-professional/cancer-statistics-for-the-uk). There is a need for new treatments, given that current standard of care for patients with metastatic disease is associated with low survival, with less than 10% living more than 2 years (1). In addition to relative resistance to conventional therapies, cancer immunotherapy (Immuno-Oncology Therapy, IOT) is also ineffective in this disease, except in the small group of patients (1-2%) with microsatellite instability/mismatch repair deficient (MSI-H/dMMR) tumours (2). Several authors consider that the reason for this resistance can be ascribed to the low mutational burden of this neoplasm, which leads to lymphocyte exclusion and anergy (3,4). However, the tumour microenvironment in PDAC has been shown to be populated by a rich variety of immune cells, but most of them bear strong immune suppressive features, which contribute to the resistance to immunotherapy (5).

The adenosine pathway is an immunosuppressive axis which has gained much attention in cancer immunology for its role in suppressing the immune activation associated with cytotoxic treatments (chemotherapy, targeted therapy and radiotherapy) (6). This has led to the clinical evaluation of inhibitors of the pathway in combination with more conventional approaches (7). The adenosine pathway involves conversion of extracellular ATP (eATP), a powerful immune activator, to extracellular adenosine (eAdo) by the ectonucleotidases CD39 and CD73 (8). eADO has been linked to cancer in several studies that have demonstrated that its concentration in different tumour tissues is several folds higher than normal tissues (6,9). CD39 is overexpressed in a subpopulation of exhausted tumour-infiltrating T-cells (10,11) and its expression correlates with another marker of immunosuppression (PD1 expression) (11). CD39 and CD73 has a role in the aggressiveness of adult glioblastoma (12), where they are

106 expressed on infiltrating macrophages (13,14). The adenosine signature recently published by
107 Sidders and colleagues (15) shows that this pathway correlates with resistance to
108 immunotherapies and is associated with other genetic features of tumour aggressiveness, such
109 as p53 mutations. The abundant presence of eAdo in the microenvironment can dampen
110 immune activation through the stimulation of a pro-tumorigenic stroma. This is mostly
111 orchestrated by macrophages and myeloid derived suppressive cells (MDSCs) (16,17),
112 favouring a tolerogenic function of dendritic cells (DCs) (18-20) which results in inhibition of
113 T-cells/NK activation (21,22).

114 The myeloid populations play a pivotal role in the aggressiveness of many cancer types
115 and in particular, pancreatic adenocarcinoma. For instance, the presence of pro-tumorigenic
116 population of macrophages (23,24) and myeloid-derived suppressive cells (MDSCs) (25)
117 infiltrating the microenvironment, is associated with a poor survival and correlates with
118 immune exclusion of PDAC. Macrophages can elicit the secretion of cytokines which can on
119 one hand, favour the proliferation and invasiveness of cancer cells while interacting with
120 cancer-associated fibroblasts (26-28), and on the other hand induce anergy and physical
121 exclusion of adaptive immune cells (29-31). Targeting macrophages in a pre-clinical
122 pancreatic cancer model has been demonstrated to be effective to obtain tumour regression and
123 reduce metastatic formation (32). Unfortunately, this approach has not translated into clinical
124 benefit, which in part can be explained by the fact that the global reduction of the tumour-
125 infiltrating macrophages can be biologically different from reprogramming distinct tumour
126 associated macrophages (TAM) subtypes (28).

127 Some recent publications link the adenosine pathway to the biology and aggressiveness
128 of PDAC, which has been shown to have an increased adenosine pathway RNA signature
129 resulting in a worse prognosis (15), and receptors for eAdo as well as CD73 have been found
130 to be overexpressed in bulk-RNA sequencing (RNAseq) when comparing tumours to normal

pancreatic tissue (33). Further, pancreatic cancer cells are known to be strongly CD73 positive (34). However, little is known about the complex mechanism generated by the adenosine pathway resulting in the immunosuppressive characteristics of pancreatic cancer microenvironment and stroma, in particular the role that the adenosine pathway has in shaping the immune infiltration of this disease.

Here, we propose a model where the tumour-infiltrating immune cell populations of PDAC cancer generate an axis of immunosuppression, where extracellular adenosine produced mostly in hypoxic regions of the tumour (identified using Mass Spectrometry Imaging), enriched for the myeloid cell infiltration, ultimately stimulates other myeloid subpopulations themselves, in particular pro-tumorigenic M2 macrophages. Blocking the adenosine pathway in an IOT-resistant PDAC model, which expresses this axis more than IOT-responsive comparator, strongly suppresses the formation of extracellular adenosine and reshapes the immune microenvironment, favouring disease control when combined with cytotoxic treatments and immunotherapies. Bulk RNAseq gene analysis confirms the role of this findings in PDAC survival, underpinning the importance of further studies for understanding the biological complexity and the clinical utility of the adenosine pathway inhibition.

Methods and materials

Cell lines and chemicals

$Kras^{LSL\text{-}G12D/+}$; $Trp53^{LSL\text{-}R172H/+}$; Pdx1-Cre; $Rosa26^{YFP/YFP}$ (KPCY)-derived cell lines 2838c3, 6499c4, 6620c1 (IOT responsive), 6419c5, 6694c2 and 6422c1 (IOT resistant) were a kind gift from Ben Stanger (University of Pennsylvania). The cell lines were obtained from single cell cloning strategy, as described previously, and were generated from tumours developed in KPCY mice with C57BL/6 background (35). Cells were grown up to 20 passages in DMEM (with pyruvate, L-glutamine and D-glucose; Gibco, #41966029) supplemented with

5% FBS (Gibco, #10270106). All the cell lines were analysed for STR fingerprinting and mycoplasma testing routinely.

Mice and *in vivo* experiments

Mice experiments were performed in the animal facility (Biological Resource Unit, BRU) of the CRUK Cambridge Institute, in accordance with the UK Animals Scientific Procedures Act 1986, with approval from the CRUK Cambridge Institute Animal Ethical Review and Welfare Body. 8-12 week old C57BL/6 mice were used for *in vivo* experiments and were purchased from Charles River (UK). $Kras^{LSL\text{-}G12D/+}$; $Trp53^{LSL\text{-}R172H/+}$; Pdx1-Cre (KPC) mice were obtained from a breeding colony maintained by the CRUK-CI Genome Editing Core team. Tumours were detected by palpation followed by ultrasound imaging by the Genome Editing Core. Tissues from KPC mice were provided once tumour dimensions or health status rendered them unsuitable for therapeutic studies. KPC mice were killed when showing clinical signs of the disease.

Tumour allograft studies were performed with technical assistance from CRUK-CI BRU staff. Mice were subcutaneously injected in the right flank with $1x10^6$ KPCY-derived cells in 50% PBS and 50% Matrigel basement membrane matrix (#354234, Corning). In the interventional experiments, mice were treated as indicated, starting 12-14 days from tumour cells implantation, to allow the microenvironment to establish. Tumour volume was calculated using the formula; $(\pi/6)*(\text{width})^2*\text{length}$. Tumour response was defined based on the % of change of the longest diameter from start of therapy (stable disease < 20% increase and < 30% decrease of target lesion RECIST v. 1.1). Mice were then killed at specific endpoints (e.g. 14 days from start of treatment) or when the tumour reached 2000 mm^3 (or before in case of appearance of clinical signs). When indicated the following drugs were used: AZD6738 (ATRi; 25 mg/kgdaily for 4 days), AZD4635 (Adora2ai; 50 mg/kg bid), 2c5mIgG1 (anti-

CD73; 10 mg/kg twice weekly), AB740080 D265A (anti-PD-L1: 10 mg/kg twice weekly), NIP228 mouse IgG1 control kappa (isotype; 10 mg/kg twice weekly) and NIP228 muIgG1 D265A (isotype; 10 mg/kg twice weekly) were provided by Astrazeneca; gemcitabine hydrochloride (Tocris, 3259) was used at 100 mg/kg twice weekly; inVivoPlus anti-CD40 (clone FGK4.5/FGK45; bioxcell BE0016-2) and InVivoPlus rat IgG2a isotype control, anti-trinitrophenol (clone 2A3; bioxcell BE0089) were used as a single injection of 100 µg. InVivoPlus anti-CTLA-4 (clone 9H10; bioxcell BP0131) or InVivoPlus isotype control polyclonal Syrian hamster IgG (bioxcell BP0087): 200 µg/dose x 3 times.

Clonogenic assay

KPCY-derived cells were seeded at 200 cells/well in a 6-well plate. After 24 hours, cells were treated with different concentrations of anti-CD73 (2c5mIgG1) antibody (1, 10, 100 µg/ml) or isotype (NIP228 mouse IgG1 control kappa) for 8 days. Antibodies were added every 3 days. On day 8, colonies were stained with SRB protocol previously described (36). Images were taken and analysed using GelCount (Oxford Optronix). Colony forming efficiency was calculated as a ratio between number of colonies and number of plated cells. Surviving fractions were calculated as the ratio between wells treated with anti-CD73 antibody and the ones treated with isotype. At least 3 wells per condition were plated for each of the 3 experimental replicates.

IncuCyte time lapse imaging

KPCY-derived cells were plated at 2500 cells/well density in a 96-well black-wall plate (at least 3 wells per condition). Cells were grown in cell culture media supplemented with the indicated concentration of anti-CD73 (2c5mIgG1) or isotype (NIP228 mouse IgG1 control kappa) antibody in triplicate. Images were acquired with 10x objective, every 3 hours from 3 different fields per well using Incucyte Live cells imaging microscope (Essen Bioscience).

Confluence was calculated as the average of the 3 fields using the Incucyte algorithm. Experiments were repeated at least 3 times.

Single cell suspension preparation

For experiments in s.c. allografts, tumours were weighed and placed in RPMI and finely minced with a scissor in a 2 ml tube which was then washed with up to 2.5 ml of digestion buffer (Tumour dissociation kit, Miltenyi, 130-096-730) plus Deoxyribonuclease I (300 µg/ml, Sigma, DN25-1G). Dissociation was performed using the protocol suggested by Miltenyi. For KPC tumours, a trypsin inhibitor (250 µg/ml, Sigma, T6522) was added to the digestion buffer. Following the digestion, the samples were passed through a 70 µM strainer filter (Grainer Bio-one, 542-070), washing with MACS buffer (PBS + 0.1% FBS and 2nM EDTA).

Spleens, inguinal and mesenteric lymph nodes were mashed on a 100 µM filter (Grainer Bio-one, 542-000) over a 50 ml tube, using a syringe plug and the filter was washed with MACS buffer and centrifuged (at 4° C as for all the following centrifugation). Red cell lysis buffer (1 ml; 0.15M Ammonium Chloride; 10mM Potassium hydrogen carbonate; 0.1mM EDTA; pH 7.4 (adjusted with KOH) was then used to resuspend splenocytes, 3 minutes at room temperature and then washed with MACS buffer and centrifuged at 300g for 5 minutes. Samples were eventually resuspended in 200-400 µl of MACS buffer.

Flow cytometry

Single cell suspensions were aliquoted in a round-bottom 96 well/plate (Costar, 3879) and stained with live/dead fixable stain (Invitrogen, L34962; 1:100 in PBS) for 10 minutes at room temperature. After washing in MACS buffer, cells were FC-blocked with anti-CD16/32 antibody (Biolegend, 101320; 1:100) for 5 minutes. Then, antibodies for surface staining were added and incubated at 4° C degrees for 30 minutes. After washing, cells were fixed with FACS fix buffer [PBS + 1% Formaldehyde + 0.02 g/ml Glucose + 0.02% Sodium Azide] for 10

minutes and then washed and resuspended in MACS buffer for FACS analysis. For intracellular staining, cells were fixed with fixation/permeabilization buffer for 15 minutes, then washed in perm buffer and stained with the relevant antibody in perm buffer for 60 minutes. Cells were then washed and resuspended in MACS buffer for FACS analysis. Samples were acquired using BD-Symphony flow cytometer and the generated FCS files were analysed using FlowJo V10 software. The following antibodies were used and gating strategies is shown in the supplementary figures: BV786-CD45 (BD Biosciences, 564225; 1:200), APC/Fire750-CD3 (Biolegend, 100248; 1:50), BV650-CD8 (Biolegend, 100741; 1:100), BV711-CD4 (Biolegend, 100549; 1:200), APC-Foxp3 (Invitrogen, 17-5773-82; 1:100) , FITC-CD19 (Biolegend, 115505; 1:200) , BV510-CD11b (Biolegend, 101245; 1:200), PerCP/Cy5.5-CD44 (Biolegend, 103031; 1:200), BV421-PD1 (Biolegend, 135218; 1:100), BV421-PD-L1 (Biolegend, 124315; 1:100), PE/Cy7-CD39 (Biolegend, 143805; 1:100), PE-CD73 (Biolegend, 127206; 1:100), FITC-F4/80 (Biolegend, 123108; 1:200), PE/Cy7-CD206 (Biolegend, 141719; 1:100), PerCP/Cy5.5-Ly6C (Biolegend, 128012; 1:100), APC/Cy7-Ly6G (Biolegend, 127624; 1:100), AF700-MHCII (Biolegend, 107629; 1:200), PE-CD11c (eBioscience, 12-0114-83; 1:200) , BV605-NKp46 (Biolegend, 137619; 1:25), APC-Adora2a (Novus Biotech, NBP1-39474APC; 1:150) , APC-CD86 (Biolegend, 105012; 1:100). Gating strategy for immune subpopulations is shown in supplementary figure 1A-B. For CD73 in vitro staining of KPCY-derived cell lines, cells were stained as described above with live/dead fixable stain and PE-CD73 antibody and analysed with BD-Symphony flow cytometer. For in vitro treatment, cells were treated with anti-CD73 (2c5mIgG1) or isotype (NIP228) antibody at a concentration of 10 µg/ml for 24 hours. Competitive staining was performed before this experiment to confirm there was no competition between 2c5mIgG1 and TY11.8 (PE-CD73) clones (data not shown).

Tissue preparation for Mass Spectrometry Imaging (MSI) and Imaging Mass Cytometry (IMC) analysis.

Tumours were snap frozen in liquid nitrogen immediately after resection and the tissues were embedded in a HPMC/PVP hydrogel as previously described (36). Sectioning was performed on a CM3050 S cryostat (Leica Biosystems, Nussloch, Germany) at a section thickness of 10 µm and the tissue sections were immediately thaw mounted and dried under a stream of nitrogen and sealed in vacuum pouches to preserve the metabolic integrity of the sections. Tissue sections for DESI-MSI and IMC were thaw-mounted onto Superfrost microscope slides (Thermo Scientific Waltham, MA, USA), whilst sections prepared for MALDI-MSI were thaw mounted onto conductive ITO coated slides (Bruker Daltonik, Bremen, Germany). Polyvinylpyrrolidone (PVP) (MW 360 kDa) and (Hydroxypropyl)-methylcellulose (HPMC) (viscosity 40-60 cP, 2 % in H2O (20 C) were purchased from Merck (Darmstadt, Germany). Methanol, water, iso-pentane and isopropyl alcohol were obtained from Fisher Scientific (Waltham, MA, USA).

Mass Spectrometry Imaging (MSI)

DESI-MSI analysis was performed on a Q-Exactive mass spectrometer (Thermo Scientific, Bremen, Germany) equipped with an automated 2D-DESI ion source (Prosolia Inc., Indianapolis, IN, USA) operated in negative ion mode, covering the applicable mass range up to a m/z of 1000, with a nominal mass resolution of 70,000. The injection time was fixed to 150 ms resulting in a scan rate of 3.8 pixel/s. The spatial resolution was adapted between experiments to allow acquisition of the data for all directly compared samples within a single experiment of 48 h, with pixel sizes ranging from 65-75 µm. A home-built Swagelok DESI sprayer was operated with a mixture of 95% methanol, 5% water delivered with a flow rate of 1.5 µL/min and nebulized with nitrogen at a backpressure of 6 bar. The resulting .raw files were converted into .mzML files using ProteoWizard msConvert (37) (version 3.0.4043) and subsequently compiled to an .imzML file (imzML converter (38) version 1.3). All subsequent

data processing was performed in SCiLS Lab (version 2021b, Bruker Daltonik, Bremen, Germany).

MALDI-MSI analysis was performed on a RapifleX Tissuetyper instrument (Bruker Daltonik, Bremen, Germany) operated in negative detection mode. 9-Aminoacridine (9-AA) prepared in 80:20 methanol:water was used as a MALDI matrix and spray deposited using an automated spray system (M3-Sprayer, HTX technologies, Chapel Hill, NC, USA). MALDI experiments were performed with a spatial resolution of 50 µm. A total of 400 laser shots were summed up per pixel to give the final spectra. For all experiments the laser was operated with a repetition rate of 10 kHz. All raw data was directly uploaded and processed in SCiLS lab (Version 2021b) software packages. All DESI and MALDI data and images were normalised to the total ion current (TIC) to compensate for signal variation across the course of the experiments. Data segmentation pipeline is shown in supplementary materials and methods.

Imaging Mass Cytometry (IMC)

Imaging mass cytometry was performed on a slide which had already been analysed by DESI-MSI. Antibodies used for IMC staining are shown in Table 1. Untagged antibodies were tagged in house, using Fluidigm Maxpar Antibody Labelling Kit, according to manufacturer's instructions. Following DESI-MSI analysis, the slide was fixed with 4% paraformaldehyde in phosphate-buffered saline (PBS) for 10 minutes. The slide was washed 3 x 5 minutes in PBS, permeabilized for 5 minutes with 1:1000 dilution of Triton X-100 in Casein Solution, washed 3 x 5 minutes in PBS, and blocked for 30 minutes with Casein Solution. Antibodies were diluted to an appropriate concentration in Casein Solution and the slide incubated overnight with the antibody solution at 4 ˚C. The slide was washed 3 x 5 minutes in PBS and nuclei were stained with DNA Intercalator-iridium at a dilution of 1:400 in PBS for 30 minutes. The slide was washed 3 x 5 minutes in PBS, 30 seconds in deionized water, then dried for storage at

room temperature until analysis. A region for IMC analysis was selected using consecutive H and E stained sections and the DESI-MSI results. A box with approximately 2 x 1.8 mm area was selected for analysis to include necrotic, necrotic margin and viable tumour regions. IMC analysis was performed using a Hyperion instrument (Fluidigm Corporation, San Francisco, CA, USA) with an ablation energy of 6 db an ablation frequency of 200 Hz. IMC images were produced using MCD viewer (Version 1.0, Fluidigm) and analysis was performed using HALO (Indica labs). Tissue regions were classified using random forest with all markers included. Cells positive for each marker were manually optimised by setting a cell intensity threshold. Values for the numbers of positive cells for markers of interest were exported for analysis in Graphpad Prism v.8

Immunohistochemistry (IHC)

Immunohistochemistry was performed as previously described in the histopathology core at the CRUK CI. Briefly, tissues were removed from the mouse at the endpoint and immediately formalin-fixed for 24 hours. Fixed tissues were then processed, embedded in paraffin and sectioned (3 µm sections). Following dewax and rehydration, as standard, antigen retrieval was performed using Leica's Epitope Retrieval Solution 2 (Tris EDTA) at 100° C for 20 minutes. Additional protein block from Dako (X090930-2) was applied. The staining using anti-mouse CD8 (Cell signalling, #98941), anti-mouse Foxp3 (Affymetrix. #14-5773) and anti-mouse p53 (Novocastra; #NCL-L-p53-CM5p) antibodies, was performed on Leica's automated Bond-III platform in conjunction with their Polymer Refine Detection System (DS9800) and a modified version of their standard template. Slides were dehydrated and cleared in xylene on Leica's automated ST5020 before sections were mounted on Leica's coverslipper, CV5030 (mounting media: DPX Mountant for Histology; Sigma Aldrich, 06522-500ML) and scanned using a ScanScopeAT2 (Aperio Leica Biosystems). Quantification of viable tumour tissue was performed after exclusion of necrotic area using the Halo software v.

3.3.2541.405 (Indica Labs). Cell density was calculated as the number of positive cells x mm2 of tumour tissue analysed. Sections of mouse spleen were used on each slide as internal control.

For the analysis of the lung metastatic burden of any individual mouse, the 4 right lobes and the left lobe were cut in multiple pieces and together fixed and then embedded, then treated as above. A p53 staining was used for helping the detection of smaller lesions (min. of 5 cells). Analysis was performed using Halo software and expressed as % of metastatic areas/total lung area analysed. Mice with intra-abdominal/thoracic organs direct infiltration were excluded from the analysis.

RNA sequencing

RNA was extracted from tumour tissues weighing up to 30 mg. Tissues were firstly disrupted and homogenised using TissueLyser II and then RNA was extracted using Qiagen RNA kit, according to manufacturer instructions. RNA was then quantified using Qubit 3.0 (life technologies) and purity and quality were assessed using Agilent 4150 (G2992AA) TapeStation system (Agilent). Library construction was followed by paired-end 50 bp sequencing on Novaseq 6000 sequencer.

Bioinformatics analysis

Sequencing files in FASTQ format were aligned against the GRCh38 mouse genome using HISAT2 with default parameters. Samtools was used to create, index and merge BAM files of reads from different lanes belonging to individual samples. FeatureCounts was utilized to quantify gene-level expression of transcripts. All downstream analyses were completed in R version 4.1.2. Prior to analysis, MSI data for sequenced samples were examined. From the vehicle-treated arm, sample 23719 showed minimal necrosis, low peri-necrotic adenosine and a high ATP/AMP ratio suggesting a very high energetic state. This identified the sample as a

potential outlier which was confirmed upon visual inspection of a PCA plot (Supplementary fig. 1C). It was excluded prior to downstream analysis.

For the remaining 11 samples, initially genes were filtered to maintain only genes that were expressed at a reasonable level in >5 treatment conditions using the filterByExpr() command from the edgeR package (ver 3.36.0) .

Differential gene expression analyses were performed on raw read counts of the combined data object of all 11 samples. To identify significantly expressed genes between treatment and control groups, we utilised a Wald test within the DESeq2 package (ver 1.34.0). Genes were considered differentially expressed when the analysis resulted in an adjusted P-value (corrected for multiple testing using the Benjamini and Hochberg method) below 0.05. The volcano plot was generated using the EnhancedVolcano package (ver 1.12.0) with the addition of custom code.

Gene set enrichment analysis (GSEA) of 712 genes identified as differentially expressed with padj≤0.05 and log2(fold change)≤-0.58 was performed via the Enrichr (suppl. table 2) server database for Kyoto Encyclopedia of Genes and Genomes (KEGG) (https://www.genome.jp/kegg/) pathways and Gene Ontology (GO): Biological Processes (http://geneontology.org/). Subsequently, enriched terms ranked for significance for each database were downloaded and are reported in Supplementary Table 4-5. Terms of interest were selected from the top 15 ranks in each table. Genes from this study which were shown to be enriched in these terms of interest were then selected to be displayed in a heatmap. Raw counts were normalised with DESeq2 prior to visualisation of gene expression levels with pheatmap (ver 1.0.12). Please refer to the supplementary methods and materials references section for all of the above.

Analysis of human PDAC available datasets and generation of PDAC-specific adenosine signature

In order to the evaluate the correlation of the adenosine-related gene expression in correlation to human PDAC we analysed 712 genes which had at least a 50% decrease (Log2FC <-0.58) following adenosine inhibition treatment, of which 561 had a human ortholog (suppl. table 2-3).

For the analysis of the adenosine-related gene expression in Bailey (39) PDAC subtypes we derived z-score of the 517 genes analysed in the dataset (out of the 561 genes) for the 97 patients with RNAseq data and subtypes information (https://www.cbioportal.org/). The z-score of all genes were summed up per each patient and the total number represented as the adenosine pathway gene score as previously shown (15) and in supplementary materials and methods.

For the generation of a PDAC-specific adenosine signature and application of this to PDAC survival, from the list of 561 human ortholog genes, we manually curated the ones related without ambiguity to the major biological processes implicated in PDAC pathogenesis and indicated by pathway analysis (hypoxia, immunity and extracellular matrix organisation). Of these genes, only those correlated positively or negatively to survival in PDAC (https://kmplot.com) and significantly co-expressed with CD73 and/or Adora2a in public datasets (Bailey et al. or TCGA) were selected. A final list of 52 genes was analysed (suppl. table 6).

Using PDAC specific data from TCGA (40) available in https://www.cbioportal.org/, we derived the z-score of these 52 genes for each patient with known disease-specific-survival (DSS), Progression free survival (PFS) and disease-free-survival (DFS). The z-scores for all genes were summed up for each patient and was deemed high adenosine score if >0 or low adenosine score if <0, as previously shown (15).

Statistics

Graphpad Prism v.8 was used for statistical analyses. Analysis and comparisons of two groups was performed with two-tailed unpaired Student's T-test when assuming Gaussian distribution or Mann Whitney test. Analysis of three or more groups was performed with one-way Anova with Tukey's multiple comparisons post-test analysis unless otherwise specified. Kaplan-Meier analysis with log-rank Mantel-Cox test was used to evaluate difference in survivals. Differences were considered significant when $p<0.05$.

Data Availability Statement

The data generated in this study are available within the article and its supplementary data files or from the corresponding authors upon reasonable request. Code for differential expression analysis and visualisation of RNAseq data is available via Github https://github.com/ka-lw/AdenoPDAC .

Results

Adenosine pathway expression on KPCY-derived cell lines

Human PDAC cells have been shown to be strongly positive for CD73 expression and have a sensitivity, although weak, to the targeting of CD73 in vitro (34). For this reason, we sought to investigate whether murine KPCY-derived cell lines (which are associated with contrasting ability to generate IOT- resistant or responsive tumours when re-implanted in syngeneic mice) express the proteins of the canonical adenosine pathway (CD39, CD73 and Adora2a). We found that, as in human cells, mouse PDAC cell lines express high levels of CD73 (from 72% to 99% of cells; fig. 1A and suppl. fig. 2A) while having negligible or no expression of CD39 and Adora2a (suppl. fig. 2B-C). Exposing the cells to an anti-CD73 antibody (2c5mIgG1) reduced significantly the detection of CD73 in all the cells after only 24-hour treatment ($p<0.05$ in all cell lines, fig. 1B), but this did not translate into inhibition of cell growth after short or long exposure at high concentrations. Indeed, confluency experiments showed that the

treatment did not affect the proliferation of any of the cell lines over a period of 72 hours (fig. 1C and suppl. fig. 2D-E), and colony-forming experiments performed on 2838c3 (IOT-responsive) and 6419c5 (IOT-resistant) clearly demonstrated no differences in terms of number or size of the colonies formed after 8 days of continuous treatment (fig. 1D and suppl. fig. 2F). In order to evaluate whether a direct effect of anti-CD73 exposure affects cell proliferation, reducing adenosine formation, we cultured KPCY-derived cell lines with increasing concentrations of AMP and 5'-N-(Ethylcarboxamido)adenosine (NECA, a stable form of adenosine). We were able to demonstrate that adenosine and AMP have no effect on the proliferation capacity of these cell lines (suppl. fig. 2G-H), corroborating the hypothesis of a non-cancer cell direct effect of anti-CD73 therapy.

Comparison between KPCY-derived cell lines allograft and KPC autochthonous tumours

Despite the lack of activity in our cell line experiments, preliminary reports from clinical trials suggest activity in patients with PDAC treated, with anti-CD73 antibody (Oleclumab) (41). As we hypothesised that this might be the result of impact on the tumour microenvironment (TME), we investigated the expression of this pathway on the tumour-infiltrating immune cells for different murine PDAC models, including KPCY-derived cell lines allografts (with differential response to IOT) and autochthonous KPC tumours. In order to understand the complexity and similarities of the immune system in these models we first compared the immune infiltration of the cell line allografts to the KPC model.

The immunosuppressive characteristics identified in autochthonous KPC tumours, appear to be more aligned with those of the IOT-resistant model. In particular regarding lymphocyte populations, KPC tumours are usually infiltrated by a low number of $CD8^+$ T cells (mean out of $CD45^+$ cells 2838c3 6.9%, 6419c5 0.9% and KPC 1.9%) which bear fewer features of activation/exhaustion (mean 70% vs 13% vs 10%) as shown in suppl. figure 3A and have a

similar regulatory T-cells (Tregs) infiltration (mean 3,2% vs 1% vs 0.7%, suppl. fig 3B) to IOT-resistant tumours. Moreover, KPC tumours showed greater heterogeneity regarding myeloid infiltrating populations (suppl. fig 3D-H) and are characterised by high M2/M1 (mean 11,3 vs 33,7 vs 24,8, suppl. fig. 3E) and $CD11b^{+}/CD11b^{-}$ dendritic cells (mean 1,3 vs 3,2 vs 4,8; suppl. fig. 3F) ratios, which are linked to an immunosuppressive and tolerogenic functionality of the TME respectively (42,43), and again this recapitulated partially the phenotype of the IOT-resistant model. Other populations such as $CD4^{+}$ T-cells, mo-MDSCs and g-MDSCs (suppl. fig. 3C, G and H) further demonstrated the diversity among KPC lesions. Taken together these results highlight that our IOT- resistant and responsive models stand out as the extreme clonotypes which can arise from a complex and heterogeneous biology which are represented in KPC autochthonous tumours.

The adenosine pathway is enriched in immune cells infiltrating PDAC models

We hypothesized that the adenosine pathway might have a more impactful role in the TME, as opposed to a cell autonomous effect. For this reason, we investigated the expression of the adenosine pathway components on tumour-infiltrating immune cells which represent significant proportion cells seen in PDAC lesions. We showed a highly significant enrichment in both the IOT-resistant and IOT-responsive models for $CD39^{+}CD73^{+}$ double-expressing immune cells, when compared to secondary lymphoid organs (spleen and nodes). In particular, the majority (65-91% in tumour vs 36-56% in spleen) of tumour-infiltrating $CD11b^{+}$ myeloid cells express the two receptors, due to an increase in expression of CD73, given that those cells are normally $CD39^{+}$ (fig. 2A-B). Similar results were shown for Tregs and $CD8^{+}$ T-cells, which are normally $CD73^{+}$ and displayed an increase in expression of CD39 in tumour, compared to the secondary lymphoid organs counterparts (suppl. fig. 4A; $p<0.05$). There was no significant difference in these findings when comparing the two models, despite their differential response to IOT. We then confirmed these findings in KPC autochthonous tumours

and found similar results, with a significant increase of CD39-CD73 double expressing $CD11b^+$ myeloid cells infiltrating the tumours compared to spleens (avg 77% vs 36% $p<0.0001$, fig. 2C-D), harvested from the same mice. Of note, 4 KPC mice had synchronous metastases (3 liver and 1 spleen), and in 3 of these, myeloid cells infiltrating the metastases were also enriched for $CD73^+CD39^+$ double expression (suppl. fig. 4 C) when compared to secondary lymphoid organs. A significant augmented co-expression was also observed for Tregs and $CD8^+$ T-cells in KPC tumours when compared to mesenteric or inguinal lymph nodes (suppl. fig. 4B). An increased percentage of CD39/CD73 double expressing CD8 T-cells and Tregs was noted in the spleens (suppl. fig. 4B) if compared to what we found in non-tumour bearing mice (not shown) or s.c. tumour bearing mice, suggesting trafficking of immune lymphoid populations between primary lesions and closer lymphoid organs.

Adenosine distributes primarily in the areas surrounding necrosis

Given the enrichment of the adenosine pathway in the TME of PDAC models, we anticipated that extracellular adenosine might have been abundant in the tumour microenvironment. Using Mass Spectrometry Imaging we evaluated the presence and the distribution of the purinergic system in the TME of IOT-resistant tumour. The tissue classification and segmentation approaches were driven by tissue-defining metabolic pattern. Areas characterised by a high energetic state defined by a high abundance of ATP and ADP and a low abundance of depleted high energy phosphates such as AMP, were called *viable tumour*. On the other hand necrotic and necrosis adjacent areas of the tissues, characterised by high abundances of lactate, products of ribonucleotide catabolism (i.e. xanthine and hypoxanthine) and other metabolites associated with tissue hypoxia and an overall energy-deprived state, were termed *necrotic margin* (fig. 3A-B). We found that adenosine is highly expressed in the microenvironment of IOT-resistant tumour, although showing a heterogenous distribution, with high abundance in the necrotic margin areas (fig. 3A,C). When we

investigated cell population distribution in the different areas using Image Mass Cytometry we noted that in the necrotic margin areas there was a massive increase in the number of infiltrating $CD11b^+$ myeloid cells, that led to a significant decrease of the ratio between cancer cells/myeloid cells (fig. 3D). This again suggests that myeloid cells have an instrumental role in the generation of adenosine in this aggressive model of PDAC.

Expression of Adora2a receptor on myeloid subpopulations of pancreatic cancer models

Having shown in these models that in the PDAC microenvironment, immunosuppressive adenosine is present abundantly, we then investigated which cells within the microenvironment might be responsive to this. We investigated the expression of the adenosine A2a receptor (Adora2a, the receptor with the highest affinity for adenosine) that has been found frequently overexpressed in human tumours. We found that Adora2a was highly expressed by tumour-infiltrating myeloid population when compared to the spleen (suppl. fig. 3D-E) and this expression was significantly higher in the IOT-resistant model in term of MFI (10000 vs 6700, $p<0.0001$) and % of $Adora2a^+$ myeloid cells (15% vs 11%, $p=0.001$). When comparing different subpopulations, pro-tumorigenic M2 macrophages, infiltrating both IOT-resistant and IOT-responsive PDAC showed high positivity for the receptor. The IOT-resistant model had higher expression of Adora2a compared to the IOT-responsive model (fig. 3E-F; $p<0.0001$) and percentage of $Adora2a^+$ M2 positivity [72% vs 43%; $p<0.0001$) (fig. 3I)]. Once more, the results were confirmed in KPC tumours where Adora2a was found to be increased in M2macrophages infiltrating the lesions when compared to matched spleens (fig. 3G-H). The KPC model demonstrated once again the heterogeneity of pancreatic lesions, which in terms of M2 macrophages positive for Adora2a receptor, covers the entire range of expression seen in the two subcutaneous models used (fig. 3I). Notably, of three KPCs where metastatic nodules were found, Adora2a expression was found retained in the M2 macrophages infiltrating the secondary lesions (suppl. fig. 4F).

In addition to pro-tumorigenic macrophages, Adora2a expression was found enriched in other myeloid immune populations infiltrating the tumours. In particular $CD11b^-$ dendritic cells, $CD11b^+$ dendritic cells (suppl. fig. 4G), M1 macrophages (suppl. fig. 4H) and mo-MDSCs (suppl. fig. 4I) express significantly higher Adora2a amount when compared to matched spleens in both models. This expression differs significantly between IOT- responsive and resistant models in $CD11b^+$ dendritic cells (mean MFI 2075 ± 174 vs 3187 ± 636 respectively; p=0.007), M1 macrophages (4521 ± 983 vs 6943 ± 1690; p=0.02) and mo-MDSCs (1894 ± 479 vs 6112 ± 1870; p=0.001) (suppl. fig. 4G-I).

Targeting adenosine pathway reshapes immune infiltration and delay tumour growth of pancreatic cancer IOT-resistant model and represents a combinational therapeutic opportunity

Our data suggest a mechanism by which the myeloid population contributes to the pro-tumorigenic functionality of the pancreatic cancer microenvironment, where eAdo generated by myeloid population and cancer cells would target and stimulate further the myeloid subpopulations, in particular the pro-tumorigenic M2 macrophages. Therefore, we inhibited *in vivo* eAdo formation and function, using an antibody against CD73 (2c5mIgG1) and a small molecule inhibitor of Adora2a (AZD4635), a combination (Adoi) which would maximise the inhibition of the axis. The 14-day treatment was started after the microenvironment was allowed to establish (12-14 days after implantation) in the IOT-resistant allografts (fig 4A). The anti-CD73 was extremely effective in reducing the expression of CD73 on the surface of all live cells (suppl. fig. 5A). Again, MSI data showed that the treatment was very effective in reducing adenosine formation in the TME (Fig. 4 B-C). In particular, adenosine was completely abolished in the viable tumour areas, while a small amount remained in the necrotic margins, although massively decreased (fig. 4C), highlighting the importance to inhibit not only the formation of adenosine through CD73 inhibition, but also targeting adenosine

545 receptors. The efficiency of the treatment on the extracellular purinergic pathway was also
546 supported by the decrease of molecules downstream adenosine (adenine and inosine in viable
547 tumour and necrotic margin areas), and the increase of upstream and alternative pathway
548 molecules as AMP (in the necrotic margin) and xanthine (in both viable tumour and necrotic
549 margin) respectively. There was no change in the distribution of ATP, ADP and hypoxanthine
550 (suppl. fig 5B).

551 The treatment led to a significant reduction of growth rate and tumour weight (fig 4D and
552 suppl. fig. 6A). The adenosine pathway has been shown to control the metastatic process and
553 several authors have shown that inhibiting this axis can reduce the metastatic burden in mice
554 models (44,45). For the first time here however, we were able to show that blocking adenosine
555 generation and function can significantly reduce the occurrence of spontaneous metastasis. The
556 6419c5 s.c. model spontaneously develops lung metastases in 100% of the mice and blocking
557 adenosine strongly reduce the metastatic burden (median of % mets/lung area 2.6% vs 0.77%;
558 p=0.016; fig. 4E).

559 These data suggest that targeting myeloid related, extracellular adenosine formation and
560 function would have an effect on tumour growth making this approach a candidate for
561 combinational therapeutic studies. Indeed, when combined with cytotoxic treatment
562 (AZD6738 and gemcitabine; fig. 4F) or IOT (anti-CD40 agonist, anti-PD-L1 and anti-CTLA4
563 (FCP); fig. 4I), the adenosine modulation reduced further the tumour growth rate of the
564 aggressive IOT-resistant 6419c5 tumour model. AZD6738/gemcitabine alone was confirmed
565 to be able to significantly slow the growth of the IOT-resistant model (2/7 stable disease, SD
566 [28.5%]), but the addition of the adenosine blocking led to a further stabilization of the tumour
567 growth in a 2-week regimen (p=0.003 vs AZD6738/gem alone; 4/7 SD [57.1%]; fig. 4G). To
568 assess whether the combination had an effect on the immune infiltration of the TME we looked
569 at IHC staining for CD8 and Foxp3 and showed that the quadruple combination almost tripled

the ratio CD8/Tregs (median 0.70 vs 0.25 of vehicles + isotype group; p=0.04; fig. 4H). The combo in fact produced a synergistic increase of CD8 infiltration (median 4.5 cells/mm^2 vs 2.7 of the control group, 3.9 of AZD6738/gem and 2.8 of AZD4635/αCD73) and reduction of Foxp3 infiltration (median 6.5 cells/mm^2 vs 8.1 of the control group, 9.3 of AZD6738/gem and 7.2 of AZD4635/αCD73) (suppl. fig. 6B-C-)

Similarly, combining adenosine blocking and FCP reduced significantly tumour growth when compared to control (65% tumour growth reduction; p=0.002) and FCP (35% tumour growth reduction; p=0.021) arms (fig. 4I-J) further increasing the tumour-infiltrating CD8/Tregs ratio induced by FPC treatment (ratio means control 0.28 vs FCP/Adoi 6.10 p=0.008; fig. 4K). Data from two separate experiments with the same controls, showed that adding Adoi to FPC remains the best combination in controlling tumour growth of the IOT-resistant 6419c5 model in syngeneic mouse (suppl. fig. 6D-F). These data taken together suggest again that targeting the adenosine pathway in PDAC offers a new strategy which can be at the crossroad of the modulation of anti-tumour immune response.

To understand the role of the adenosine modulation in reprogramming the TME, given the effect on tumour growth alone or in combination we analysed the changes in immune infiltration following anti-CD73 and AZD4635 treatment. Flow cytometry analysis showed that following treatment, tumours were less likely to be infiltrated by M2 macrophages (median approximately 35000 vs 23000 cells/100mg; p=0.002; fig. 5A-B), in particular PD-$L1^+$ ones (median 79% vs 65%; p=0.002; fig. 5B). IMC analysis revealed that the reduction of M2 macrophages either F4/80^+ $CD206^+$ (fig. 5C,E) and $CD68^+$ $CD206^+$ (fig. 5D-F) cells, was more prominent in the viable tumour areas. Notably this reduced infiltration is present in areas other than those where adenosine is abundant, suggesting that adenosine is stimulating the production of factors affecting recruitment of macrophages in the viable tumour areas. Blocking the axis, also led to a reduced frequency of Tregs out of CD4+ T-cells infiltration (mean 42% vs 27%;

p=0.03, fig. 5G-H) and a strong reduction of PD-L1 expression for all live cells within the tumour (p=0.0006), in particular $CD45^+$ cells (p=0.008) as shown in suppl. fig. 7A. The expression of PD-L1 however declined for $F4/80^+$ macrophages (p=0.02) but not for dendritic cells following treatment (suppl. fig. 7B). Finally, IMC data also confirmed a reduction of total macrophages in the treated tumours as shown by flow, again more evident in the viable tumour regions (fig. 5C-D, F4/80 and CD68 panels and suppl. fig 7C). IMC also showed a global reduction of what we indicated as M1 macrophages ($F4/80^+$ $CD206^-$ $MHCII^+$) (suppl. fig. 7 D-E) which was not appreciated in the flow analysis, and a total increase of granzyme B (GrB) infiltrating cells following treatment (data not shown), in particular $CD4^+$ GrB^+ cells (suppl. fig. 7 F-G), the latest also called cytolytic CD4 T-cells, recently associated to the response to cancer immunotherapy (46). Further studies would further shed light on the relevance of these results, analysing the contribution of adenosine abundance and spatial distribution to modelling of tumour infiltration by distinct macrophage subpopulations beyond M1-M2 dichotomy.

We next looked at single agent contribution and found that a significant tumour growth inhibition compared to control was only achieved when the combination of AZD4635 and anti-CD73 antibody was used (p=0.003; suppl. fig. 7H). Regarding the TME, only the full combination was able to reduce the M2 macrophage infiltration (p=0.03, suppl. fig I) and the ratio M2/M1 macrophages (p=0.04; suppl. fig 7J) in the tumour. Further, additive effect of double inhibition was seen for the reduction of tumour infiltrating Tregs (suppl. fig. 7K).

RNA sequencing analysis reveals reprogramming of TME following adenosine modulation

The TME of PDAC is an intricated structure that relies on the presence of multiple non-malignant cells. This TME is well recapitulated in pre-clinical models of PDAC (35). In order to investigate the broader effect of Adoi in 6419c5 PDAC model, given the effect we have seen

in the infiltrating immune suppressive populations, we performed a bulk RNAseq analysis of the 6419c5 model treated with Adoi or control (5 vs 6 mice, see methods). Following the 14-day treatment with Adora2a inhibitor and anti-CD73 a total of 712 genes had at least a 50% decrease (logfold <-0.58; fig. 6A). KEGG and GO Biological process pathway analysis revealed a profound dependency of the TME on the presence of extracellular adenosine (fig. 6B-C). Genes associated with hypoxia response and vasculogenesis (e.g. Hif1a, Slc2a1, Hilpda, Adm, Vegfa, Vegfd), immunity and immune suppression (e.g. Cd274, Cd209, Mrc1, Cd200, Il1a, Il6, Ptgs2) and tumour stroma/ECM organisation (e.g. Col5a3, Col6a3, Itga2, Mmp13, Mmp3, Mmp9, Ereg, Pthlh) were significantly downregulated by the treatment (fig. 6 C). Of note, several functional and structural genes associated with different subtypes of M2 macrophages (Cd209, Mrc1) were found to be decreased, supporting data from flow and IMC data analysis. As already indicated by the flow analysis, RNAseq analysis also showed a significant decrease of the expression of Cd274 (PD-L1) gene, suggesting a strong rational of the use of adenosine inhibition as combination for immunotherapy studies involving immune checkpoint inhibitors. Adenosine signalling pathway expression has previously been associated with the presence of hypoxia (47,48); here we show for the first time that the presence of functional extracellular adenosine pathway is responsible for the expression of several genes related to hypoxia (including Hif1a) in a positive feedback loop.

To evaluate the importance of this pathway in the context of human PDAC and highlight the role in the formation of TME we scored our adenosine-related gene expression set with the PDAC subtypes published by Bailey (39). Of our 712 genes with a 50% decrease, 561 had a human ortholog and of these the z-scores of 517 genes were summed in each of the 97 patients with RNAseq data in Bailey et al. to obtain a score. We were able to show that the adenosine-related gene expression is mostly expressed in the aggressive squamous subtype (fig. 6D), that has been originally associated with a poorer prognosis when compared to others.

The score remained significantly higher even when comparing the squamous subtypes with the grouped non-squamous (fig. 6E).

In order to create a PDAC-specific adenosine signature and to evaluate its performance in PDAC-specific outcomes, we created a signature starting from the 561 human ortholog genes with a 50% decreased following Adoi treatment. Of these, 52 genes were selected for the signature (fig. 6F), that according to our RNAseq dataset were clearly associated with the pathway areas dependent on adenosine (hypoxia response, immunity, tumour stroma), were associated positively or negatively with PDAC prognosis, and were significantly co-expressed with CD73 and/or Adora2a in the PDAC genome datasets (TCGA or Bailey). Of the 176 and 170 patients with available progression free survival (PFS) and disease-specific survival (DSS) outcome respectively, we found that the presence of a high adenosine signature is associated with higher probability of PDAC progression (mPFS high Ado 13.05 vs low Ado 18.25, p=0.02; fig. 6G) and a poorer PDAC-specific survival (mDSS high Ado 19.66 vs low Ado *NR*, p=0.01; fig. 6H), suggesting again that the presence of a functional adenosine pathway has a detrimental role in human PDAC. These data should be considered in light of the fact that patients in TCGA dataset are predominantly non-metastatic, and the presence of the adenosine signature seems to become relevant for PDAC associated death 20 months after diagnosis. Notably, the presence of a high adenosine signature is also associated with shorter disease-free-survival (mDFS high ado 23.54 vs low Ado 49.68, p=ns; suppl. fig. 7L).

Overall these data highlight the role of the innate immune system in shaping a pro-tumorigenic, immune suppressive microenvironment in PDAC, dependent on the formation of extracellular adenosine in the context of a hypoxic milieu. We can speculate that this unfavourable environment may create the condition for a more aggressive PDAC phenotype which would then translate in the ability to escape the immune system, resist to cytotoxic treatment and easily metastasize.

669 # Discussion

670 Pancreatic ductal adenocarcinoma (PDAC) is projected to become the second highest
671 cause of cancer-related death in the US within 10 years (49), and represents one of the major
672 unmet needs of cancer treatment. Despite extensive efforts by laboratory and clinical scientists
673 in the last 50 years, only 1% of patients diagnosed with PDAC today will survive for 10 years
674 (https://www.cancerresearchuk.org/health-professional/cancer-statistics-for-the-uk). The
675 response rate following standard treatments is poor, usually short-lasting, and associated with
676 significant treatment related toxicity (1). In the past few years, immunotherapy has provided
677 new hope in the treatment of several types of cancer, and has dramatically changed the life
678 expectancy of many patients with metastatic disease (50). However, this has not been true for
679 patients with PDAC which is associated with a very low response rate to immunotherapy,
680 usually confined to MSI-H/dMMR tumours, rarely found in this disease (2).

681 The role of the innate immune system in the generation of an immune suppressive/pro-
682 tumorigenic microenvironment in PDAC is well known. The presence of marked infiltration
683 of macrophages has been identified as an independent predictive factor of the aggressiveness
684 and prognosis of PDAC, in patients (23,24). Only recently, three phase I clinical trials in
685 patients with PDAC have shown that targeting the innate immune system can have impact in
686 patients with PDAC. A phase I trial published on Lancet Oncology, showed that a combination
687 of anti PD-1 and CD40 agonist, added to gemcitabine and nab-paclitaxel, led to 60% of
688 response rate, with some durable responses (51). In addition, the inhibition of the
689 CXCL12/CXCR4 axis has been demonstrated to modify the immunosuppressive TME of
690 PDAC and CRC patients (52,53).

691 The extracellular adenosine pathway has also been shown to influence the TME
692 fostering the immune suppression provided by some innate immune subpopulations (as

myeloid and NKs) and inhibiting the function of the adaptive immune system, in particular, T-cells (6,33,44). By activating its receptors, adenosine is able to increase the intracellular concentration of cAMP which leads to the induction of a M2 phenotype of macrophages and block the secretion of IL1β increasing the release of CXCL1, IL-6, IL-10 and IL-8 among others from myeloid population which are known to orchestrate immune exclusion (8,54). eAdo also favours the formation and maintenance of Treg cells (8), which are known to favour cancer progression and IOT resistance .

Emerging data correlate the adenosine pathway to the promotion and aggressiveness of PDAC. CD73 is also overexpressed on the surface of cancer cells of PDAC (34,55), but its role on cancer cells is controversial, as is the cancer cell direct role of extracellular adenosine. A recent publication, shows that genomic targeting on mouse PDAC cells of CD73 leads to a reduced in vivo tumour formation and change in the circulating and infiltrating immune system (57). Data from bulk RNA-sequencing have determined that CD73 along with Adora2a and Adora2b are strongly overexpressed in tumours when compared to normal pancreatic tissue (33). Recently an adenosine signature has been published which clearly identifies enrichment in PDAC and a correlation with progression free survival as well as overall survival (15).

To date, little was known about the expression of the adenosine pathway in the context of the innate and adaptive immune system in PDAC, how the extracellular adenosine is generated and what are the targets of adenosine also in regard to its spatial distribution and formation of adenosine.

Our results show for the first time, that the mechanism of generation of extracellular adenosine in pancreatic cancer TME is finely orchestrated by tumour infiltrating myeloid cells and tumour cells, due to the expression of high level of CD39 in infiltrating myeloid cells and CD73 on both cell types. We have also demonstrated that the pathway can be overexpressed

in T-cells infiltrating the tumours, regardless of their activation status (fig. 1,2 and suppl. fig. 2,4). The distribution of extracellular adenosine is spatially heterogeneous and a high level of extracellular adenosine correlates with the presence of a hypoxic environment and is favoured by the presence of necrosis, where the myeloid population is enriched (fig.3). Necrosis is common in human PDAC and related to poor prognosis for all stages (56). The enrichment of a $CD39^+$ $CD73^+$ double population, potentially able to independently produce adenosine, does not seem to correlate with IOT- resistant or responsive tumour models, but there is a difference when the target of adenosine (Adora2a receptor), is considered. Adora2a on myeloid populations, in particular in pro-tumorigenic M2 macrophages but also in antigen presenting cells, is differentially expressed in regard of IOT response phenotype, with the resistant tumours abundantly overexpressing the receptor in these populations (fig.3 and suppl. fig. 4). The bulk RNAseq analysis of tumour treated with adenosine inhibition revealed indeed a broader role for adenosine in PDAC TME (fig. 6). Genes related to immunosuppression and innate immunity recruitment (Cd274, Csf2, Cxcl2, Ccl3, Ccl4, Ccl12, Il1a, Osm, Il6), angiogenesis (Vegfa, Vegfd, Adm2, Flt1, Pgf, Egln1) and cell-ECM interaction (Adam19, Adamts14, Adamts4, Adamts5, Col5a3, Col6a, Itga2, Itga7, Mmp3, Mmp9, Mmp12) indicated the targeting of population of cells responsible for the acquisition of a pro-tumorigenic, pro-metastatic, pro-fibrotic and immune resistant phenotype. Further, the downregulation of genes associated with hypoxia (Hif1a, Hilpda, Nos2, Hk1, Hk2, Egln3) following treatment shows not only that the adenosine pathway is induced during hypoxia (e.g. CD73 and Adora2b), but that the hypoxia response is also dependent on the presence of the adenosine pathway in what we can speculate is a positive feedback loop. The inhibition of adenosine led to a reduced infiltration of M2 macrophages further from the hypoxic regions where adenosine is most abundant, suggesting that the effect of adenosine is stimulating the secretion of factors that are recruiting monocytes into the tumour microenvironment, replenishing macrophage infiltration

(fig. 5 and suppl. fig. 7). Notably, targeting the pathway can reduce tumour growth in an IOT-resistant model, improving the response to cytotoxic and immunotherapy combinations (fig. 4 and suppl. fig. 6)

Targeting adenosine would represent an alternative strategy to reduce the infiltration of pro-tumorigenic macrophages in PDAC lesions. One approach has been the administration of a CSF1R inhibitor (32), which has shown promising pre-clinical data, that have not been translated in human so far. A recent publication shows that in CRC mouse models, the use of anti CSF1R treatment spares a subpopulation of macrophages characterised by the expression of Cd274 (PD-L1), Vegfa, Hilpda, Bhlhe40, Mmp12, Cebpb, Hmox1 among others (28). Given that all of these genes are among the immune suppressive and vasculogenic molecules that seem to be strongly downregulated by adenosine inhibition and our data show a reduction of some subpopulation of PD-L1^{+} macrophages, we can speculate that adenosine inhibition could potentially target these populations of pro-angiogenesis, immune suppressive macrophages.

Information provided by the PDAC specific adenosine signature, indicated that the adenosine pathway seems to play a peculiar role in progression and survival of human PDAC, due to the ability of the adenosine inhibition to profoundly reprogram the tumour microenvironment in PDAC models (fig. 6 and suppl. fig. 7). Gathering more information on the role of this pathway in human cancers should be a priority, retrospectively evaluating and then prospectively stratifying the patients on the basis of histopathological/radiological features and the spatial distribution of adenosine. We could expect that efficiently targeting the adenosine pathway may potentially be at the crossroads of cytotoxic and immunotherapy efficacy and the exploration of these strategies is needed in PDAC-specific clinical trials. These would not only need to be designed to target the generation of adenosine through CD73 inhibition but also adenosine specific receptors.

In summary, we have shown that tumour-infiltrating myeloid immune cells contribute to the generation of extracellular adenosine in the context of PDAC, and that this correlates with the presence of hypoxia. Macrophages in particular, express high levels of Adora2a receptor in PDAC models and targeting the adenosine/myeloid axis delays PDAC tumour growth, improving the efficacy of cytotoxic and immunotherapies. Finally, data from IMC, flow cytometry and RNAseq suggest that the adenosine pathway is fundamental for the formation of a pro-tumorigenic, immunosuppressive TME, and its expression is associated with an aggressive phenotype and poor survival in human PDAC.

Acknowledgments

All CRUK CI authors received research funding from Cancer Research UK (Nos. C14303/A17197 and C9545/A29580). The Li Ka Shing Centre where this work was performed was generously funded by CK Hutchison Holdings Limited, the University of Cambridge, CRUK, The Atlantic Philanthropies and others. This work was supported by Cancer Research UK (C9685/A27444) to VG. The authors wish to thank all the CRUK Cambridge Institute core facilities, in particular Research Instrumentation & Cell Services (RICS), Flow Cytometry, Histopathology, Biological Resource Unit (BRU), Genomics and Genome editing cores. VG would like to thank Maike de la Roche (CRUK Cambridge Institute - University of Cambridge) and Klaus Okkenhaug (Department of Pathology - University of Cambridge) for helpful suggestions and advices. This study was also supported by Cancer Research UK Precision Panc grant C96/A25238. HB holds a PhD studentship at the University of Cambridge which is supported jointly by the University of Cambridge Experimental Medicine Training Initiative (EMI) programme in partnership with AstraZeneca (EMI-AZ) and the NIHR Biomedical Research Centre and SYL is founded by the Cambridge Trust (Cambridge International

791 Scholarship). Work by JT / KW is funded by a core grant award from the MRC
792 (MC_UU_00025/12). The KPCY-derived cell lines were a kind gift of Ben Stanger
793 (University of Pennsylvania). AZD4635, AZD6738 and the antibodies anti-CD73 (2C5,
794 murine IgG1-Fc), anti-PD-L1 (AB740080 D265A), NIP228 muIgG1 isotype, NIP228 muIgG1
795 D265A isotype, were kindly provided by Astrazeneca. The results shown here are in part based
796 upon data generated by the TCGA Research Network: https://www.cancer.gov/tcga.

797

798 Figure legends

799 Figure 1. Expression of CD73 on KPCY-derived cell lines and response to anti-CD73 in
800 vitro inhibition.

801 (A) Representative histogram of CD73 expression on KPCY-derived cell line in flow
802 cytometry. (B) CD73 expression was evaluated on KPCY-derived cell lines after 24 hours
803 incubation with 10 μg/ml of anti-CD73 or isotype.
804 (C) 6419c5 (upper) and 2838c3 (lower) cell lines were grown with increasing concentration of
805 anti-CD73 or isotype (100 μg/ml) and confluency was evaluated using IncuCyte time lapse
806 imaging for up to 72 hours. For each experiment, 3 different wells per condition were used.
807 (D-E) Representative image (D) and graphs (E) showing survival fraction of cells (2838c3 left,
808 6419c5 right) from colony-forming experiment following 8-day treatment with anti-CD73 or
809 isotype. For each experiment, 3 different wells per condition were used.
810 All data are presented as mean ± SEM and were repeated 3 times. Statistical analysis was
811 performed with two-tailed unpaired Student's t-test (B), mixed-effect model (C) and one-way
812 Anova with post-test analysis for multiple comparisons; p values are shown in the graphs when
813 considered significant ($p<0.05$).

814

Figure 2. The adenosine pathway members are expressed on PDAC-infiltrating immune cells.

(A) Representative flow cytometry plots showing expression of CD39 and CD73 on myeloid population (left), Tregs (middle) and CD8+ T-cells (right) from KPCY-cell line derived tumour (upper) and matched spleen (lower) (N= 5 mice per group).

(B) Box and whisker graph showing $CD39^{+}CD73^{+}$ double expression on $CD11b^{+}$ cells for 2838c3 and 6419c5 in tumours, matched spleens and tumour draining lymph nodes.

(C-D) Representative flow cytometry plots (C) and box and whisker graph (D) showing $CD39^{+}CD73^{+}$ double expression on $CD11b^{+}$ cells infiltrating autochthonous KPC tumours. All data are presented as interleaved box and whiskers.

Statistical analysis was performed using one-way Anova with post-hoc test analysis for multiple comparisons (B) and two-tailed unpaired Student's t-test (D); p values are shown in the graphs when considered significant ($p<0.05$).

Figure 3. Adenosine distribution is spatially heterogeneous and targets myeloid subpopulations.

(A) Mass spectrometry Imaging (MSI) representative images showing adenosine expression and distribution in PDAC allografts (4 mice per group) at day 21 post-implantation. Classification was obtained based on metabolites expression and are represented as follows: viable tumour (red), necrotic margins (blue).

(B) Relative tissue composition differences of viable tumour, necrotic margin and necrotic areas for 6419c5 and 2838c3 allografts at day 21 post-implantation. As shown, necrosis was present in only one 2838c3 sample at 21 days post-implantation.

(C) MSI analysis showing relative abundance (a.u.) of adenosine in the different areas in 6419c5 and 2838c3 at day 21 post-implantation. Bars represent means.

(D) The plot (upper left) shows cell density of the ratio cancer cells (PanCK$^+$, purple) / myeloid cells (CD11b$^+$, blue) on a Log2 scaled plot from Imaging Mass cytometry (IMC). The results of the comparison between the whole area analysed and the other tissue regions are not shown. N = 6. Asterisks ****, show adjusted p value of <0.0001. The IMC and tissue segmentation images (upper right and lowers) are from one 6419c5 representative biological replicates at day 28 post-implantation. The tissue segmentation of the IMC image was performed by Random Forest Classification using all markers analysed. Scale bar on the IMC image is 200 µm. Segmentation shows viable tumour (green), necrosis (yellow), necrotic margin (blue) and off-tissue (red).

(E-F) Representative plot (E) and summary graph (F) from flow cytometry analysis showing Adora2a expression on pro-tumorigenic M2 macrophages in allografts (upper) derived from 6419c5 (left) and 2838c3 (right) implantation. Same expression is shown in M2 macrophages in matched spleens (lower) (8-9 mice per group were used).

(G-H) Flow cytometry plot (G) and graph (H) showing expression of Adora2a in M2 macrophages comparing KPC (n=8) autochthonous tumours and matched spleens.

(I) Box and whisker plot of the percentage of M2 macrophages positive for Adora2a comparing two allografts (6419c5 and 2838c3) and KPC tumours.

Statistical analysis was performed using one-way Anova with post-hoc test analysis for multiple comparisons (D,F,I) and two-tailed unpaired Student's t-test (H); p values are shown in the graphs when considered significant ($p<0.05$).

Figure 4. In vivo modulation of the adenosine pathway reduces tumour growth and metastasis and improves the efficacy of cytotoxics and cancer immunotherapy.

(A) Schedule of adenosine inhibition (Adoi) treatment. Treatment was started following 12-14 days from implantation and continued for 2 weeks. Antibody anti-CD73 (2c5, murine IgG1)

was dosed twice per week intraperitoneally at 10 mg/kg. Adora2a inhibitor (AZD4635) was given by oral gavage twice daily at 50 mg/kg.

(B-C) Mass spectrometry Imaging (MSI) representative images (B) and MSI analysis graph with relative abundance (a.u.) (C) showing adenosine expression and distribution in PDAC allografts treated with vehicle + isotype or Adoi, at day 14 from treatment start. Classification was obtained based on metabolites expression and are represented as follows: viable tumour (green line), necrotic margins (yellow line).

(D) Tumour growth ratio (left) and weight (right) of 6419c5 allografts in C57Bl/6 mice treated with anti-CD73 + AZD4635 (N=16) or vehicles + isotypes (N=15).

(E) Representative image (left) and graph (right) showing % of area of the lung analysed occupied by metastasis (met/lung areas x 100) in vehicle + isotype (N=12) and anti-CD73+AZD4635 (N=13), evaluated for the presence of spontaneous occurrence of lung metastases. Every plot represents a single mouse. Tissues were stained with an anti-p53 antibody to highlight the presence of cancer cells. A group of more than 5 p53-positive cells was counted as metastasis.

(F) Schedule (left) and tumour growth ratio (right) of 6419c5 tumour allografts treated as following (N=7 mice per group): vehicles + isotype, AZD6738 + gemcitabine, anti-CD73 + AZD4635, AZD6738 + gemcitabine + anti-CD73 + AZD4635. (G) Percentage change in the long diameter length following 14 days of treatment per group. Number of mice with stable disease (SD, <20% increase and <30% decrease) are shown at the bottom.

(H) Immunohistochemistry analysis following treatment in F showing ratio of $CD8^+/Foxp3^+$ cells.

(I) Schedule (left) and tumour growth ratio (right) of 6419c5 tumour allografts treated as following (N=5 mice per group): vehicle + isotypes, FCP (anti-CD40 agonist, anti-CTLA4, anti PD-L1), anti-CD73 + AZD4635 (Adoi), FPCAdoi.

(J) Percentage change in the long diameter length following 14 days of treatment per group. Number of mice with stable disease (SD, <20% increase and <30% decrease) are shown at the bottom.

(K) Immunohistochemistry analysis following treatment in I showing ratio of $CD8^+/Foxp3^+$ cells. All data are presented as mean ± SEM. Statistical analysis was performed using Mann-Whitney test (D-E), mixed-effect model (F-I) and one-way Anova with post-hoc test analysis for multiple comparisons (C,H-K); p values are shown in the graphs when considered significant ($p<0.05$).

Figure 5. Adenosine inhibition remodels the PDAC tumour microenvironment reducing pro-tumorigenic macrophages and Tregs.

(A) Representative flow cytometry plot showing tumour associated macrophages (TAM) infiltrating 6419c5 allografts following 14 day of treatment with vehicle + isotype (left panel) or anti-CD73 + AZD4635 (right panel).

(B) M2 macrophage allograft infiltration (left, number of cells/100 mg of tumour) and (right) percentage of M2 macrophages positive for PD-L1 (8 and 10 mice per group analysed).

(C-D) Representative IMC image of F4/80 and CD206 (C) and CD68 and CD206 (D) positive cells infiltrating 6419c5 allograft merged (1^{st} panel of C and D) or not with segmentation following Adoi (lower panels) or control (upper). The tissue segmentation of the IMC image was performed by Random Forest Classification using all markers analysed. Scale bar on the IMC image is 200 µm. Segmentation shows viable tumour (green), necrosis (yellow), necrotic margin (blue) and off-tissue (red).

(E-F) The bar plot shows cell density (number of cells per mm2) of $F480^+CD206^+$ cells (E) and $CD68^+CD206^+$ (F) per segment area.

(G) Representative flow cytometry plot showing regulatory T-cells (Tregs) infiltrating 6419c5 allografts following 14 day of treatment with vehicle + isotype (left panel) or anti-CD73 + AZD4635 (right panel).

(H) Infiltration of allografts by Tregs (number of cells/100mg of tumour; 8 and 10 mice per group analysed).

All data are represented as box and whisker plots. Statistical analysis was performed using Mann-Whitney test (B-H) and one-way Anova with post-hoc test analysis for multiple comparisons (E-F); p values are shown in the graphs when considered significant ($p<0.05$).

Figure 6 RNA sequencing demonstrates a crucial role for the adenosine pathway in the modelling of the TME, and its correlation to human PDAC prognosis.

(A) Volcano plot related to 6419c5 allografts. Gene overexpressed in vehicle + isotype arm are on the left side (blue dots), and genes overexpressed in the anti-CD73 + AZD4635 arm (Adoi, orange dots).

(B) Enrichment bar plot of significant overexpressed pathways in the vehicle + isotype group (adenosine high), according to KEGG and GO Biological process.

(C) Heatmaps showing genes regulated during treatment (light grey for controls, dark grey for Adoi) which are part of the significantly different pathways according to KEGG (left) and GO Biological process (right). Some genes are shown in both heatmaps

(D-E) Human ortholog genes with a 50% downregulation following 14 days of Adoi, were scored using z-score derived from Bailey's subtypes dataset. Genes scores comparing Adex, immunogenic, squamous and pancreatic progenitor (D) or squamous vs non-squamous (E) are shown.

(F) PDAC-specific gene signature of 52 genes used for analysis of TCGA human PDAC dataset, related to the main pathways implied (immunity, hypoxia response and tumour stroma).

(G-H) Gene signature applied to PDAC TCGA dataset (G) for progression free survival (176 patients) and (H) disease specific survival (170 patients) Kaplan-Meier. All data are presented as mean ± SEM when applicable.

Statistical analysis was performed using one-way Anova with post-hoc test analysis for multiple comparisons (D), two-tailed unpaired Student's t-test (E) and log-rank Mantel-Cox test to evaluate difference in survivals (G-H); p values are shown in the graphs when considered significant ($p<0.05$).

References

Cancer Research UK, https://www.cancerresearchuk.org/health-professional/cancer-statistics/statistics-by-cancer-type/pancreatic-cancer, Accessed March 2022

1. Conroy T, Desseigne F, Ychou M, Bouche O, Guimbaud R, Becouarn Y*, et al.* FOLFIRINOX versus gemcitabine for metastatic pancreatic cancer. N Engl J Med **2011**;364(19):1817-25 doi 10.1056/NEJMoa1011923.
2. Le DT, Durham JN, Smith KN, Wang H, Bartlett BR, Aulakh LK*, et al.* Mismatch repair deficiency predicts response of solid tumors to PD-1 blockade. Science **2017**;357(6349):409-13 doi 10.1126/science.aan6733.
3. Hu ZI, Shia J, Stadler ZK, Varghese AM, Capanu M, Salo-Mullen E*, et al.* Evaluating Mismatch Repair Deficiency in Pancreatic Adenocarcinoma: Challenges and Recommendations. Clin Cancer Res **2018**;24(6):1326-36 doi 10.1158/1078-0432.CCR-17-3099.
4. Balachandran VP, Luksza M, Zhao JN, Makarov V, Moral JA, Remark R*, et al.* Identification of unique neoantigen qualities in long-term survivors of pancreatic cancer. Nature **2017**;551(7681):512-6 doi 10.1038/nature24462.
5. Ho WJ, Jaffee EM, Zheng L. The tumour microenvironment in pancreatic cancer - clinical challenges and opportunities. Nat Rev Clin Oncol **2020**;17(9):527-40 doi 10.1038/s41571-020-0363-5.
6. Antonioli L, Blandizzi C, Pacher P, Hasko G. Immunity, inflammation and cancer: a leading role for adenosine. Nat Rev Cancer **2013**;13(12):842-57 doi 10.1038/nrc3613.

7. Augustin RC, Leone RD, Naing A, Fong L, Bao R, Luke JJ. Next steps for clinical translation of adenosine pathway inhibition in cancer immunotherapy. J Immunother Cancer **2022**;10(2) doi 10.1136/jitc-2021-004089.
8. Cekic C, Linden J. Purinergic regulation of the immune system. Nat Rev Immunol **2016**;16(3):177-92 doi 10.1038/nri.2016.4.
9. Goodwin KJ, Gangl E, Sarkar U, Pop-Damkov P, Jones N, Borodovsky A*, et al.* Development of a quantification method for adenosine in tumors by LC-MS/MS with dansyl chloride derivatization. Anal Biochem **2019**;568:78-88 doi 10.1016/j.ab.2018.11.004.
10. Duhen T, Duhen R, Montler R, Moses J, Moudgil T, de Miranda NF*, et al.* Co-expression of CD39 and CD103 identifies tumor-reactive CD8 T cells in human solid tumors. Nat Commun **2018**;9(1):2724 doi 10.1038/s41467-018-05072-0.
11. Simoni Y, Becht E, Fehlings M, Loh CY, Koo SL, Teng KWW*, et al.* Bystander CD8(+) T cells are abundant and phenotypically distinct in human tumour infiltrates. Nature **2018**;557(7706):575-9 doi 10.1038/s41586-018-0130-2.
12. Ott M, Tomaszowski KH, Marisetty A, Kong LY, Wei J, Duna M*, et al.* Profiling of patients with glioma reveals the dominant immunosuppressive axis is refractory to immune function restoration. JCI Insight **2020**;5(17) doi 10.1172/jci.insight.134386.
13. Takenaka MC, Gabriely G, Rothhammer V, Mascanfroni ID, Wheeler MA, Chao CC*, et al.* Control of tumor-associated macrophages and T cells in glioblastoma via AHR and CD39. Nat Neurosci **2019**;22(5):729-40 doi 10.1038/s41593-019-0370-y.
14. Goswami S, Walle T, Cornish AE, Basu S, Anandhan S, Fernandez I*, et al.* Immune profiling of human tumors identifies CD73 as a combinatorial target in glioblastoma. Nat Med **2020**;26(1):39-46 doi 10.1038/s41591-019-0694-x.
15. Sidders B, Zhang P, Goodwin K, O'Connor G, Russell DL, Borodovsky A*, et al.* Adenosine Signaling Is Prognostic for Cancer Outcome and Has Predictive Utility for Immunotherapeutic Response. Clin Cancer Res **2020**;26(9):2176-87 doi 10.1158/1078-0432.CCR-19-2183.
16. Cekic C, Day YJ, Sag D, Linden J. Myeloid expression of adenosine A2A receptor suppresses T and NK cell responses in the solid tumor microenvironment. Cancer Res **2014**;74(24):7250-9 doi 10.1158/0008-5472.CAN-13-3583.
17. Sorrentino C, Miele L, Porta A, Pinto A, Morello S. Myeloid-derived suppressor cells contribute to A2B adenosine receptor-induced VEGF production and angiogenesis in a mouse melanoma model. Oncotarget **2015**;6(29):27478-89 doi 10.18632/oncotarget.4393.
18. Li L, Huang L, Ye H, Song SP, Bajwa A, Lee SJ*, et al.* Dendritic cells tolerized with adenosine A(2)AR agonist attenuate acute kidney injury. J Clin Invest **2012**;122(11):3931-42 doi 10.1172/JCI63170.
19. Borodovsky A, Barbon CM, Wang Y, Ye M, Prickett L, Chandra D*, et al.* Small molecule AZD4635 inhibitor of A2AR signaling rescues immune cell function including CD103(+) dendritic cells enhancing anti-tumor immunity. J Immunother Cancer **2020**;8(2) doi 10.1136/jitc-2019-000417.
20. Wilson JM, Kurtz CC, Black SG, Ross WG, Alam MS, Linden J*, et al.* The A2B adenosine receptor promotes Th17 differentiation via stimulation of dendritic cell IL-6. J Immunol **2011**;186(12):6746-52 doi 10.4049/jimmunol.1100117.
21. Romio M, Reinbeck B, Bongardt S, Huls S, Burghoff S, Schrader J. Extracellular purine metabolism and signaling of CD73-derived adenosine in murine Treg and Teff cells. Am J Physiol Cell Physiol **2011**;301(2):C530-9 doi 10.1152/ajpcell.00385.2010.
22. Cekic C, Linden J. Adenosine A2A receptors intrinsically regulate CD8+ T cells in the tumor microenvironment. Cancer Res **2014**;74(24):7239-49 doi 10.1158/0008-5472.CAN-13-3581.
23. Ino Y, Yamazaki-Itoh R, Shimada K, Iwasaki M, Kosuge T, Kanai Y*, et al.* Immune cell infiltration as an indicator of the immune microenvironment of pancreatic cancer. Br J Cancer **2013**;108(4):914-23 doi 10.1038/bjc.2013.32.

24. Steele NG, Carpenter ES, Kemp SB, Sirihorachai V, The S, Delrosario L*, et al.* Multimodal Mapping of the Tumor and Peripheral Blood Immune Landscape in Human Pancreatic Cancer. Nat Cancer **2020**;1(11):1097-112 doi 10.1038/s43018-020-00121-4.
25. Zhang Y, Velez-Delgado A, Mathew E, Li D, Mendez FM, Flannagan K*, et al.* Myeloid cells are required for PD-1/PD-L1 checkpoint activation and the establishment of an immunosuppressive environment in pancreatic cancer. Gut **2017**;66(1):124-36 doi 10.1136/gutjnl-2016-312078.
26. Raghavan S, Winter PS, Navia AW, Williams HL, DenAdel A, Lowder KE*, et al.* Microenvironment drives cell state, plasticity, and drug response in pancreatic cancer. Cell **2021**;184(25):6119-37 e26 doi 10.1016/j.cell.2021.11.017.
27. Zhu Y, Herndon JM, Sojka DK, Kim KW, Knolhoff BL, Zuo C*, et al.* Tissue-Resident Macrophages in Pancreatic Ductal Adenocarcinoma Originate from Embryonic Hematopoiesis and Promote Tumor Progression. Immunity **2017**;47(3):597 doi 10.1016/j.immuni.2017.08.018.
28. Zhang L, Li Z, Skrzypczynska KM, Fang Q, Zhang W, O'Brien SA*, et al.* Single-Cell Analyses Inform Mechanisms of Myeloid-Targeted Therapies in Colon Cancer. Cell **2020**;181(2):442-59 e29 doi 10.1016/j.cell.2020.03.048.
29. Beatty GL, Winograd R, Evans RA, Long KB, Luque SL, Lee JW*, et al.* Exclusion of T Cells From Pancreatic Carcinomas in Mice Is Regulated by Ly6C(low) F4/80(+) Extratumoral Macrophages. Gastroenterology **2015**;149(1):201-10 doi 10.1053/j.gastro.2015.04.010.
30. Ruffell B, Chang-Strachan D, Chan V, Rosenbusch A, Ho CM, Pryer N*, et al.* Macrophage IL-10 blocks CD8+ T cell-dependent responses to chemotherapy by suppressing IL-12 expression in intratumoral dendritic cells. Cancer Cell **2014**;26(5):623-37 doi 10.1016/j.ccell.2014.09.006.
31. Daley D, Mani VR, Mohan N, Akkad N, Pandian G, Savadkar S*, et al.* NLRP3 signaling drives macrophage-induced adaptive immune suppression in pancreatic carcinoma. J Exp Med **2017**;214(6):1711-24 doi 10.1084/jem.20161707.
32. Candido JB, Morton JP, Bailey P, Campbell AD, Karim SA, Jamieson T*, et al.* CSF1R(+) Macrophages Sustain Pancreatic Tumor Growth through T Cell Suppression and Maintenance of Key Gene Programs that Define the Squamous Subtype. Cell Rep **2018**;23(5):1448-60 doi 10.1016/j.celrep.2018.03.131.
33. Allard B, Allard D, Buisseret L, Stagg J. The adenosine pathway in immuno-oncology. Nat Rev Clin Oncol **2020**;17(10):611-29 doi 10.1038/s41571-020-0382-2.
34. Zhou L, Jia S, Chen Y, Wang W, Wu Z, Yu W*, et al.* The distinct role of CD73 in the progression of pancreatic cancer. J Mol Med (Berl) **2019**;97(6):803-15 doi 10.1007/s00109-018-01742-0.
35. Li J, Byrne KT, Yan F, Yamazoe T, Chen Z, Baslan T*, et al.* Tumor Cell-Intrinsic Factors Underlie Heterogeneity of Immune Cell Infiltration and Response to Immunotherapy. Immunity **2018**;49(1):178-93 e7 doi 10.1016/j.immuni.2018.06.006.
36. Dannhorn A, Kazanc E, Ling S, Nikula C, Karali E, Serra MP*, et al.* Universal Sample Preparation Unlocking Multimodal Molecular Tissue Imaging. Anal Chem **2020**;92(16):11080-8 doi 10.1021/acs.analchem.0c00826.
37. Adusumilli R, Mallick P. Data Conversion with ProteoWizard msConvert. Methods Mol Biol **2017**;1550:339-68 doi 10.1007/978-1-4939-6747-6_23.
38. Race AM, Styles IB, Bunch J. Inclusive sharing of mass spectrometry imaging data requires a converter for all. J Proteomics **2012**;75(16):5111-2 doi 10.1016/j.jprot.2012.05.035.
39. Bailey P, Chang DK, Nones K, Johns AL, Patch AM, Gingras MC*, et al.* Genomic analyses identify molecular subtypes of pancreatic cancer. Nature **2016**;531(7592):47-52 doi 10.1038/nature16965.
40. Liu J, Lichtenberg T, Hoadley KA, Poisson LM, Lazar AJ, Cherniack AD*, et al.* An Integrated TCGA Pan-Cancer Clinical Data Resource to Drive High-Quality Survival Outcome Analytics. Cell **2018**;173(2):400-16 e11 doi 10.1016/j.cell.2018.02.052.
41. Overman MJ, LoRusso P, Strickler JH, Patel SP, Clarke SJ, Noonan AM*, et al.* Safety, efficacy and pharmacodynamics (PD) of MEDI9447 (oleclumab) alone or in combination with

durvalumab in advanced colorectal cancer (CRC) or pancreatic cancer (panc). Journal of Clinical Oncology **2018**;36(15_suppl):4123- doi 10.1200/JCO.2018.36.15_suppl.4123.

42. Poh AR, Ernst M. Tumor-Associated Macrophages in Pancreatic Ductal Adenocarcinoma: Therapeutic Opportunities and Clinical Challenges. Cancers (Basel) **2021**;13(12) doi 10.3390/cancers13122860.

43. Kenkel JA, Tseng WW, Davidson MG, Tolentino LL, Choi O, Bhattacharya N*, et al.* An Immunosuppressive Dendritic Cell Subset Accumulates at Secondary Sites and Promotes Metastasis in Pancreatic Cancer. Cancer Res **2017**;77(15):4158-70 doi 10.1158/0008-5472.CAN-16-2212.

44. Yan J, Li XY, Roman Aguilera A, Xiao C, Jacoberger-Foissac C, Nowlan B*, et al.* Control of Metastases via Myeloid CD39 and NK Cell Effector Function. Cancer Immunol Res **2020**;8(3):356-67 doi 10.1158/2326-6066.CIR-19-0749.

45. Sun X, Wu Y, Gao W, Enjyoji K, Csizmadia E, Muller CE*, et al.* CD39/ENTPD1 expression by CD4+Foxp3+ regulatory T cells promotes hepatic metastatic tumor growth in mice. Gastroenterology **2010**;139(3):1030-40 doi 10.1053/j.gastro.2010.05.007.

46. Cachot A, Bilous M, Liu YC, Li X, Saillard M, Cenerenti M*, et al.* Tumor-specific cytolytic CD4 T cells mediate immunity against human cancer. Sci Adv **2021**;7(9) doi 10.1126/sciadv.abe3348.

47. Synnestvedt K, Furuta GT, Comerford KM, Louis N, Karhausen J, Eltzschig HK*, et al.* Ecto-5'-nucleotidase (CD73) regulation by hypoxia-inducible factor-1 mediates permeability changes in intestinal epithelia. J Clin Invest **2002**;110(7):993-1002 doi 10.1172/JCI15337.

48. Philip K, Mills TW, Davies J, Chen NY, Karmouty-Quintana H, Luo F*, et al.* HIF1A up-regulates the ADORA2B receptor on alternatively activated macrophages and contributes to pulmonary fibrosis. FASEB J **2017**;31(11):4745-58 doi 10.1096/fj.201700219R.

49. Rahib L, Smith BD, Aizenberg R, Rosenzweig AB, Fleshman JM, Matrisian LM. Projecting cancer incidence and deaths to 2030: the unexpected burden of thyroid, liver, and pancreas cancers in the United States. Cancer Res **2014**;74(11):2913-21 doi 10.1158/0008-5472.CAN-14-0155.

50. Mellman I, Coukos G, Dranoff G. Cancer immunotherapy comes of age. Nature **2011**;480(7378):480-9 doi 10.1038/nature10673.

51. O'Hara MH, O'Reilly EM, Varadhachary G, Wolff RA, Wainberg ZA, Ko AH*, et al.* CD40 agonistic monoclonal antibody APX005M (sotigalimab) and chemotherapy, with or without nivolumab, for the treatment of metastatic pancreatic adenocarcinoma: an open-label, multicentre, phase 1b study. Lancet Oncol **2021**;22(1):118-31 doi 10.1016/S1470-2045(20)30532-5.

52. Biasci D, Smoragiewicz M, Connell CM, Wang Z, Gao Y, Thaventhiran JED*, et al.* CXCR4 inhibition in human pancreatic and colorectal cancers induces an integrated immune response. Proc Natl Acad Sci U S A **2020**;117(46):28960-70 doi 10.1073/pnas.2013644117.

53. Bockorny B, Semenisty V, Macarulla T, Borazanci E, Wolpin BM, Stemmer SM*, et al.* BL-8040, a CXCR4 antagonist, in combination with pembrolizumab and chemotherapy for pancreatic cancer: the COMBAT trial. Nat Med **2020**;26(6):878-85 doi 10.1038/s41591-020-0880-x.

54. Fong L, Hotson A, Powderly JD, Sznol M, Heist RS, Choueiri TK*, et al.* Adenosine 2A Receptor Blockade as an Immunotherapy for Treatment-Refractory Renal Cell Cancer. Cancer Discov **2020**;10(1):40-53 doi 10.1158/2159-8290.CD-19-0980.

55. King RJ, Shukla SK, He C, Vernucci E, Thakur R, Attri KS*, et al.* CD73 induces GM-CSF/MDSC-mediated suppression of T cells to accelerate pancreatic cancer pathogenesis. Oncogene **2022**;41(7):971-82 doi 10.1038/s41388-021-02132-6.

56. Hiraoka N, Ino Y, Sekine S, Tsuda H, Shimada K, Kosuge T*, et al.* Tumour necrosis is a postoperative prognostic marker for pancreatic cancer patients with a high interobserver reproducibility in histological evaluation. Br J Cancer **2010**;103(7):1057-65 doi 10.1038/sj.bjc.6605854.

Figure 1

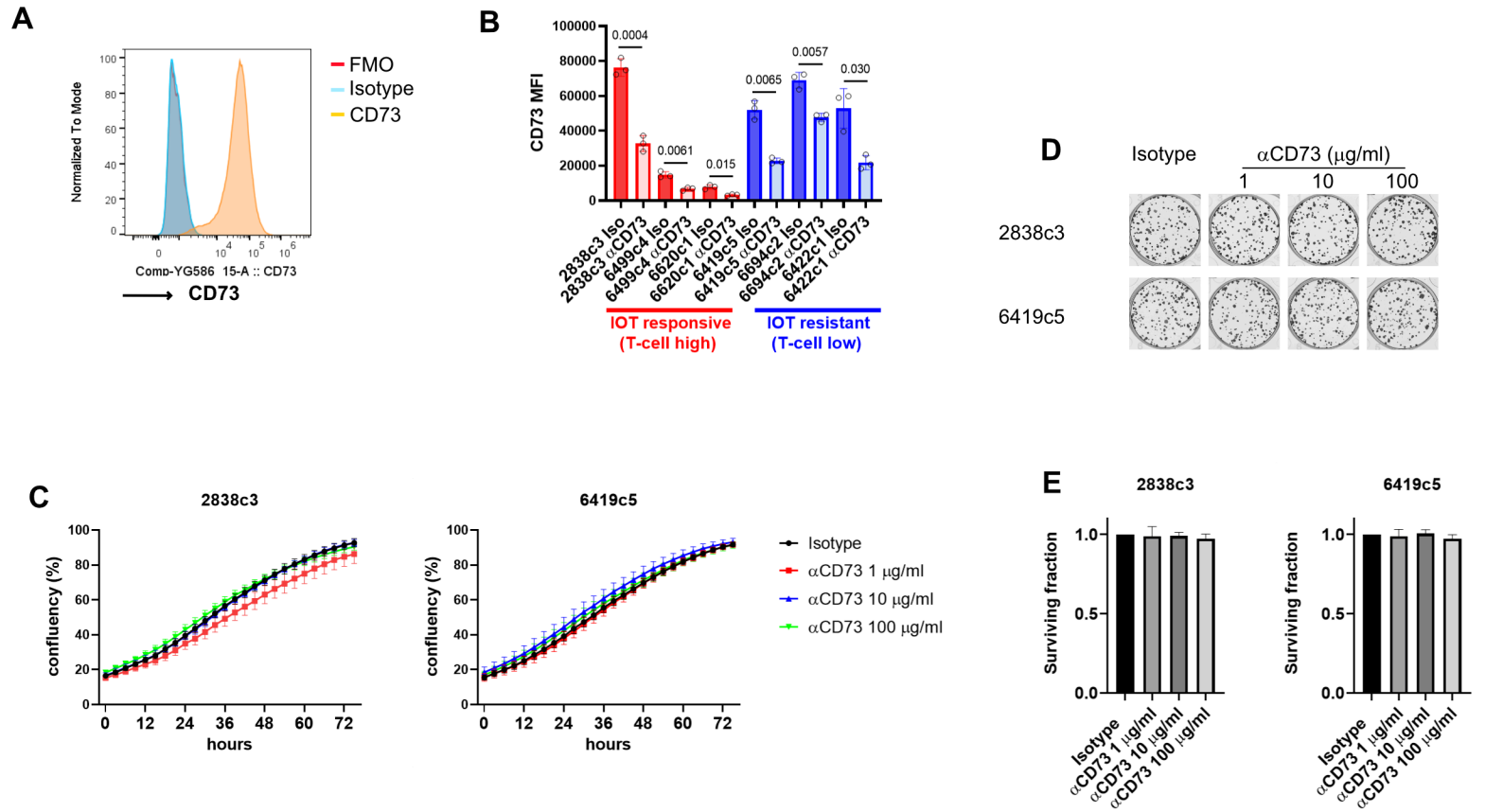

Figure 2

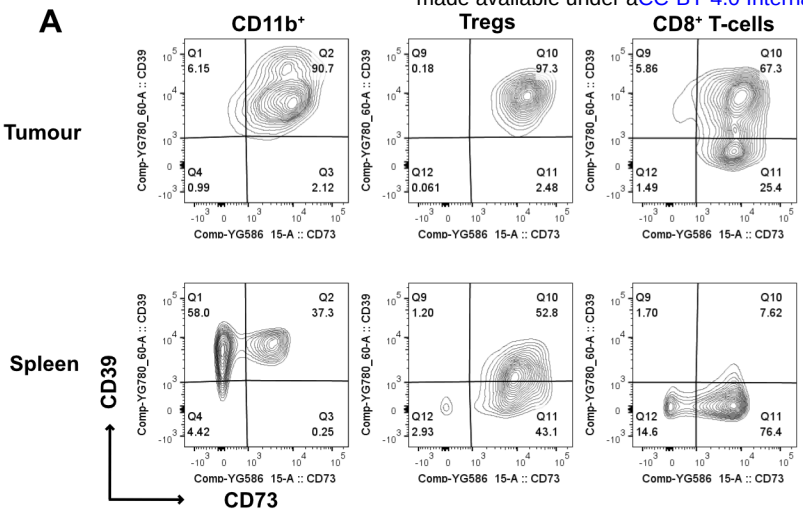

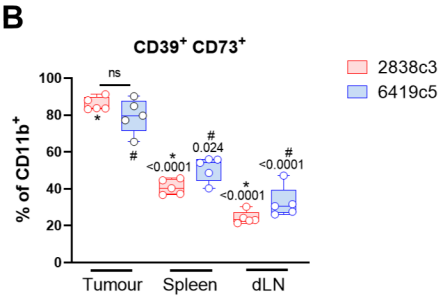

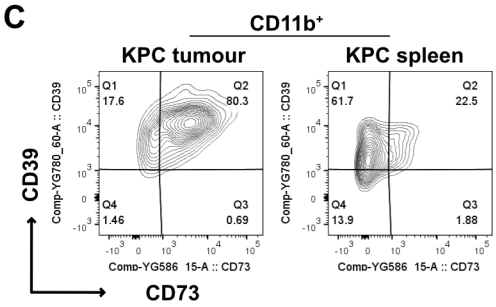

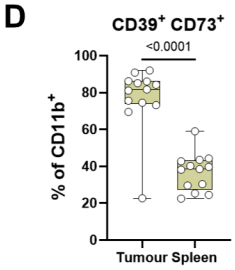

Figure 3

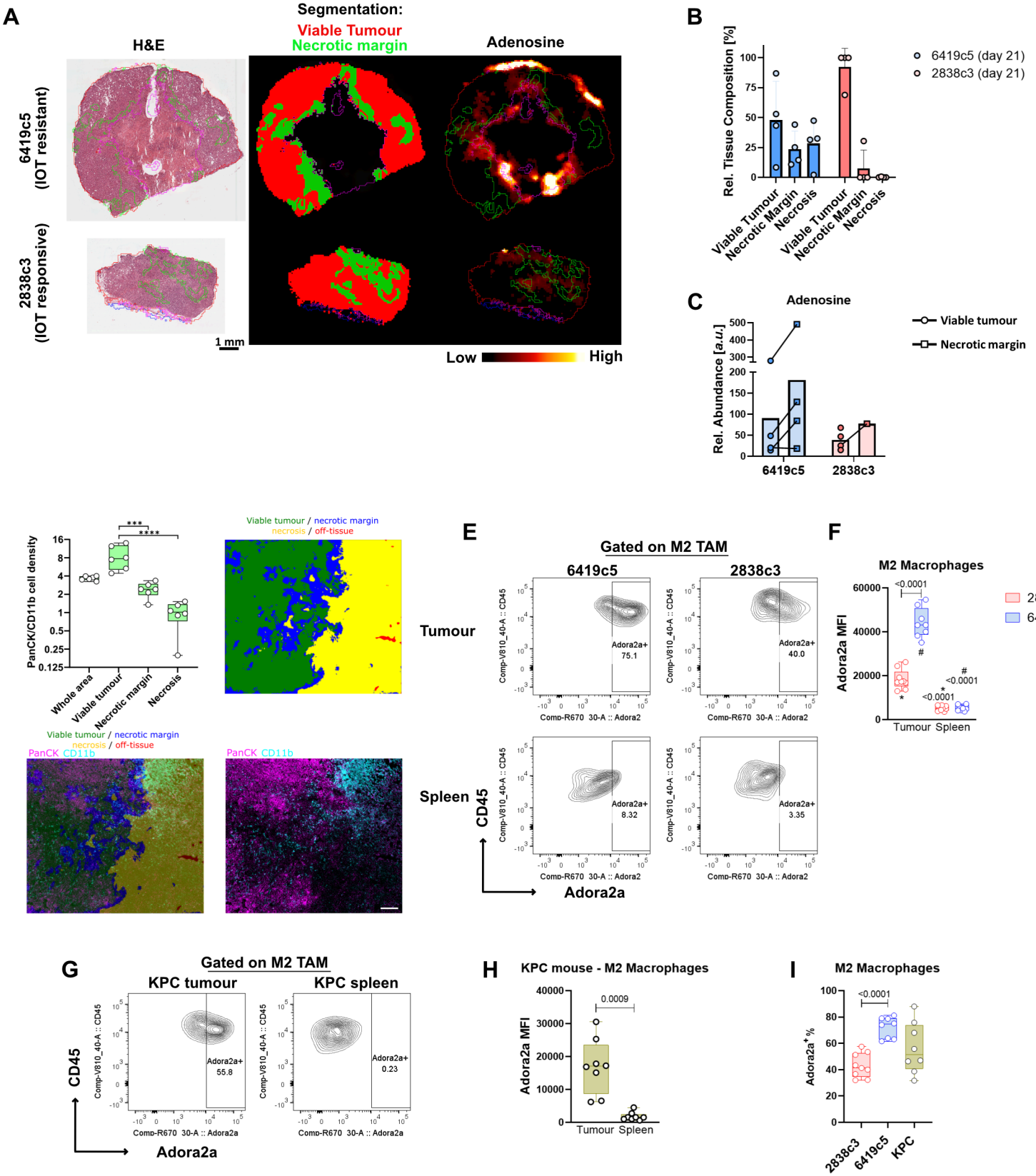

Figure 4

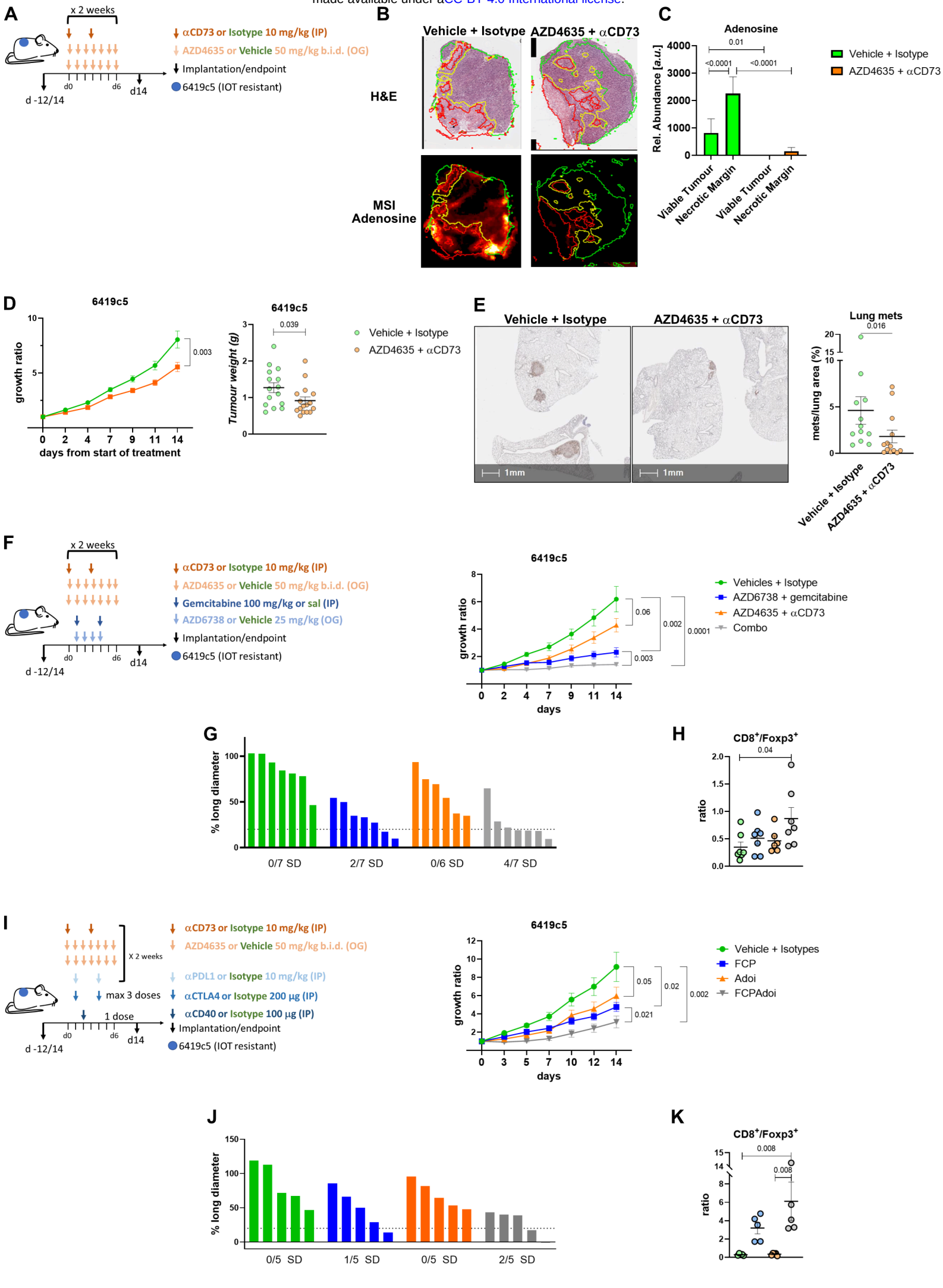

Figure 5

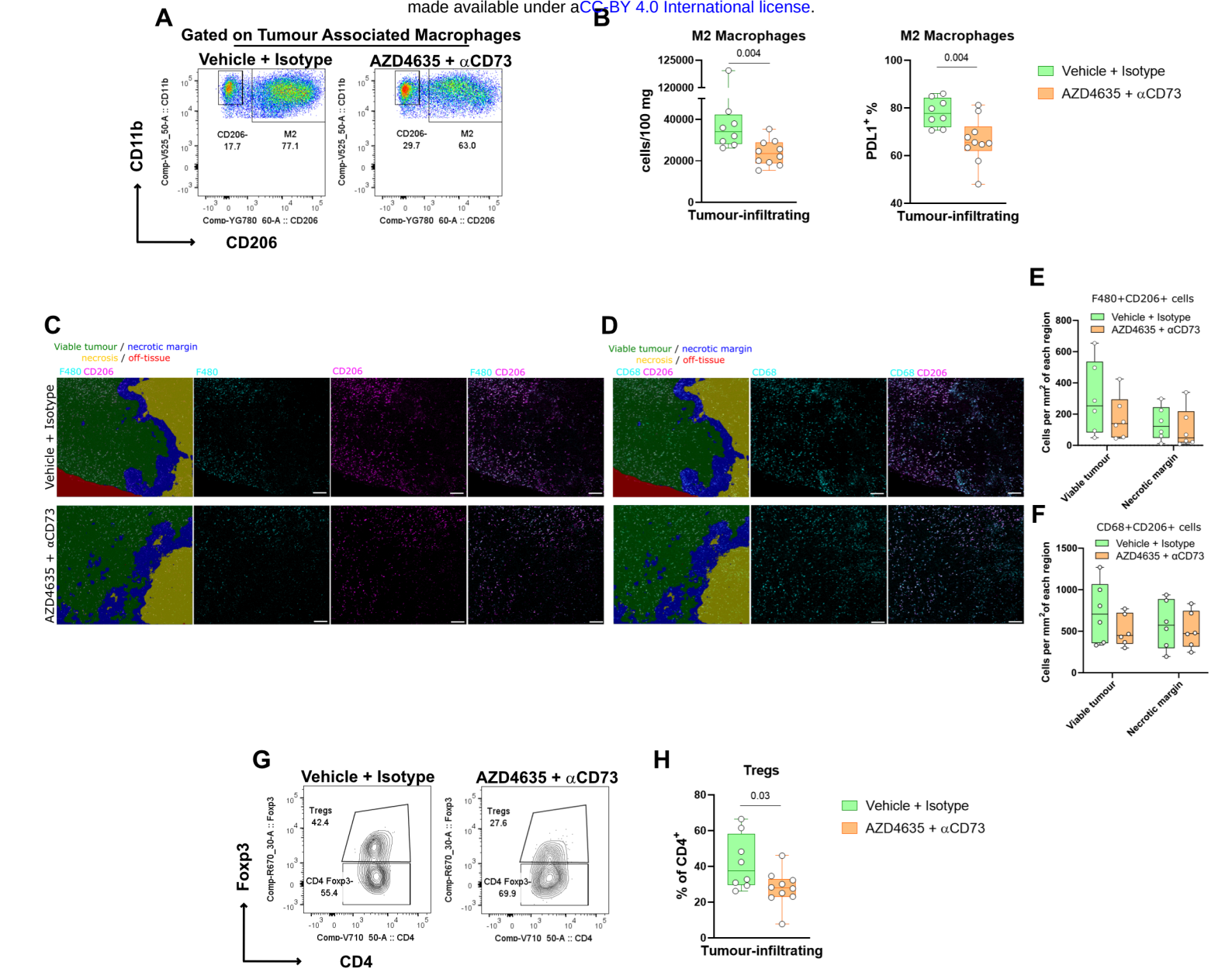

Figure 6